Wannier orbital theory and angle-resolved photoemission spectroscopy for the quasi-one-dimensional conductor $LiMo_6O_{17}$. III. The two metallic bands in the gap

L. Dudy
Randall Laboratory, University of Michigan, Ann Arbor, Michigan 48109, USA;
Physikalisches Institut und Röntgen Center for Complex Material Systems, Universität Würzburg, D-97074 Würzburg, Germany;
and Synchrotron SOLEIL, L'Orme des Merisiers, 91190 Saint-Aubin, France

J. W. Allen
Randall Laboratory, University of Michigan, Ann Arbor, Michigan 48109, USA

J. D. Denlinger
Advanced Light Source, Lawrence Berkeley National Laboratory, Berkeley, California 94270, USA

J. He*
Department of Physics and Astronomy, Clemson University, Clemson, South Carolina 29534, USA

M. Greenblatt
Department of Chemistry & Chemical Biology, Rutgers University, 123 Bevier Rd. Piscataway, New Jersey 08854, USA

M. W. Haverkort
Max-Planck-Institut für Festkörperforschung, Heisenbergstrasse 1, D-70569 Stuttgart, Germany;
Max-Planck-Institut für Chemische Physik fester Stoffe, Nöthnitzer Str. 40, D-01187 Dresden, Germany;
and Institut für Theoretische Physik, Universität Heidelberg, Philosophenweg 16, D-69120 Heidelberg, Germany

Y. Nohara and O. K. Andersen
Max-Planck-Institut für Festkörperforschung, Heisenbergstrasse 1, D-70569 Stuttgart, Germany

(Received 27 March 2023; revised 4 December 2023; accepted 13 December 2023; published 21 March 2024)

This is the third paper of a series of three papers presenting a combined study by band theory and angle-resolved photoemission spectroscopy (ARPES) of lithium purple bronze. The first paper laid the foundation for the theory, and the second paper discussed a general comparison between theory and experiment, including deriving an ARPES selection rule. The present paper III focuses in detail on the two metallic, quasi-one-dimensional (quasi-1D) *xy*-like bands left in the 0.4 eV dimerization gap between the *xz* and *yz* valence and conduction (V&C) bands. The hybridizations with the latter change the perpendicular dispersions of — and splitting between — the resulting $\widetilde{xy}$ bands. The edges of the V (C) bands, in particular, push resonance peaks up (down) in the $\widetilde{xy}$ bands which are now described by a two-band Hamiltonian whose two first terms consist of the pure *xy* block of the six-band tight-binding (TB) Hamiltonian and whose four following terms describe the resonant coupling to (i.e., indirect hopping via) the V&C bands. The two-band Hamiltonian extends the selection rule derived in the previous paper to the hybridized $\widetilde{xy}$ bands, which enables extracting the split quasi-1D Fermi surface (FS) from the raw ARPES data. The complex shape of the FS, verified in detail by our ARPES, depends strongly on the Fermi-energy position in the gap, implying a great sensitivity to Li stoichiometry of properties dependent on the FS, such as FS nesting or superconductivity. The strong resonances prevent either a two-band TB model or a related real-space ladder picture from giving a valid description of the low-energy electronic structure. Down to a temperature of 6 K, we find no evidence for a theoretically expected downward renormalization of perpendicular single-particle hopping due to LL fluctuations in the quasi-1D chains.

DOI: 10.1103/PhysRevB.109.115145

I. INTRODUCTION

This last paper in a series of three about angle-resolved photoemission spectroscopy (ARPES) and Wannier orbital (WO) theory of the quasi-one-dimensional (quasi-1D) conductor $LiMo_6O_{17}$ deals with the Fermi surface (FS) formed by the two metallic *xy*-like bands (the $\widetilde{xy}$ bands) in the gap caused by the *c*-axis dimerization [Sec. I III A][1] between

*Deceased.

[1]I and II refers to sections, figures, and equations in papers I [1] and II [2], respectively.

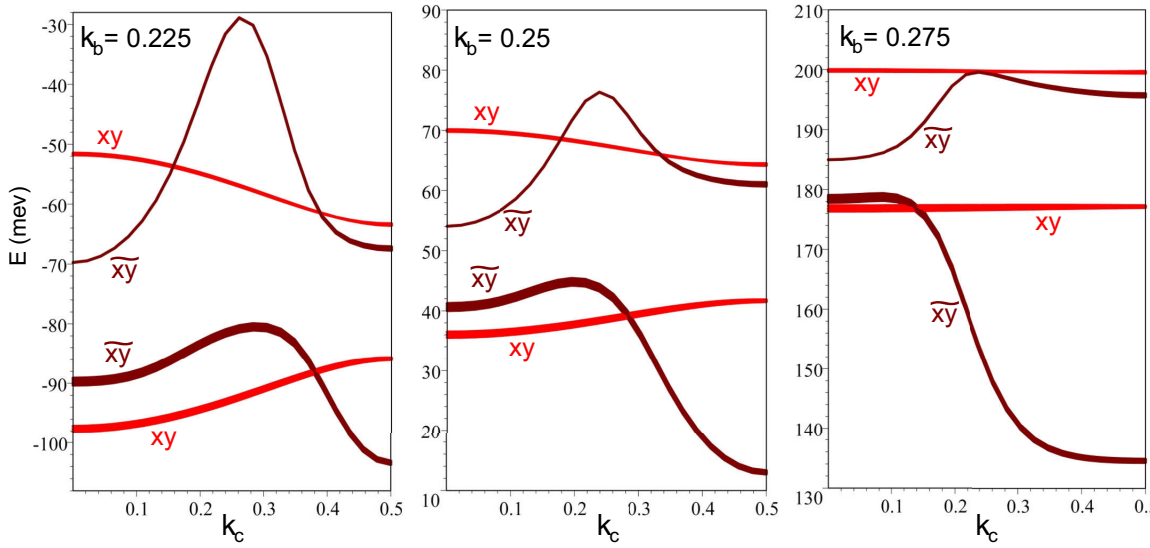

FIG. 1. The two quasi-1D metallic bands in the gap between the valence (V) and conduction (C) bands as functions of the perpendicular k_c in the irreducible BZ, $0 \leqslant k_c < 0.5$, and for k_b fixed at 0.225, 0.250, and 0.275. The red bands are the pure xy bands and the dark-red $\widetilde{xy}$ bands include the hybridization with the four V&C bands. The extra fatness (band decoration) is proportional to the $|\mathbf{k}\rangle$ character, which for the dark-red bands was obtained from the two-band Hamiltonian (4). The red and the dark-red fat bands for $k_b = 0.225$ were already shown in, respectively, Figs. I 6 and I 7, and their $|\mathbf{k}\rangle$ characters in the middle and bottom parts of Fig. II 4. The upper and lower $\widetilde{xy}$ bands as functions of (k_b, k_c) are shown on the left-hand side of Fig. 3. The ARPES-refined tight-binding (TB) parameter values I (43)–I (46) were used and the xz-yz hybridization [parameters I (40)] was neglected.[2] The value of E in the denominators of Eq. (4) were iteratively adjusted to equal the eigenvalue in question of the two-band Hamiltonian whereby it equals the appropriate eigenvalue of the six-band Hamiltonian [with the values I (47) of the xz-yz parameters set to zero]. The energy is in meV with respect to the center of the gap. The top of the valence band and the bottom of the conduction band are $\pm 2G_1 = \mp 218$ meV and the ARPES samples had $E_F = 75$ meV.

the xz- and yz-like valence and conduction (V&C) bands. All six t_{2g} bands, half of them filled in the stoichiometric compound, were studied by band theory in paper I [1]. In paper II [2], we compared the theory with the experiment (by ARPES) for the filled bands. There, also a WO theory of the experimentally found ARPES intensity variations was derived and applied.

As a basis for the initial states we used the six t_{2g} WOs, $w_m(\mathbf{r})$, and $W_m(\mathbf{r})$ with $m = xy$, xz, and yz, centered respectively on Mo1 and MO1, the most central molybdenums of the lower and the upper strings, $^{\text{Mo2}}\diagdown_{\text{Mo1}}\diagup^{\text{Mo4}}\diagdown_{\text{Mo5}}$ and $^{\text{MO5}}\diagdown_{\text{MO4}}\diagup^{\text{MO1}}\diagdown_{\text{MO2}}$, wiggling around the $\mathbf{c}+\mathbf{a}$ direction perpendicular to $\mathbf{b}$, the direction of the quasi-1D conductivity [see Chart I (15), and Figs. I 2 and I 9]. Due to the approximate translational equivalence of $w_m(\mathbf{r})$ and $W_m(\mathbf{r})$ [see Eqs. I (17) and I (18)], the photoemission intensity is essentially the projection of the initial-state band onto the *pseudo* Bloch sum $|\mathbf{k}\rangle$, defined by Eq. I (52). Such a pseudo Bloch sum is a periodic function of $\mathbf{k}$ in the *double* zone [see Fig. I 8 or II 1], i.e., the zone of the undimerized lattice [the one with primitive translations $\mathbf{a}$, $(\mathbf{c}+\mathbf{b})/2$, and $(\mathbf{c}-\mathbf{b})/2$, and reciprocal translations $\mathbf{a}^*$, $\mathbf{c}^*+\mathbf{b}^*$, and $\mathbf{c}^*-\mathbf{b}^*$]. The other basis function is simply $|\mathbf{k}+\mathbf{c}^*\rangle$. In the absence of c-axis dimerization, $w_m(\mathbf{r})$ and $W_m(\mathbf{r})$ are identical, apart from a phase factor, and the $|\mathbf{k}\rangle$ and the $|\mathbf{k}+\mathbf{c}^*\rangle$ band structures are each periodic in the double zone and translated by $\mathbf{c}^*$, i.e., by $\Delta k_c = 1$, with respect to each other. In the presence of dimerization, the basis functions become linearly independent and will mix near the crossings of the $|\mathbf{k}\rangle$ and $|\mathbf{k}+\mathbf{c}^*\rangle$ band structures, which will now gap and thereby restore the single-zone periodicity [see Figs. I 6, I 7, and I 4].

This description of the band structure in paper I, followed by the theory of the ARPES intensity variations in paper II, explains our comprehensive set of ARPES data for the occupied bands (Figs. II 10, II 11, II 12, and II 14), including the observations that the intensity follows the $|\mathbf{k}\rangle$ character (Fig. II 4) and of a surprisingly strong photon-energy dependence of the photoelectron intensity from the FS (Fig. II 9). The former means that the ARPES intensity is enhanced for the lower-energy band in the first- and is extinguished in the second physical zone; conversely for the higher-energy band, if occupied [Fig. II 4]. The latter leads us to use $h\nu = 33$ eV for the FS studies to be described in the present paper III, Sec. III.

Figure II 14 demonstrated that refinement of merely 7 of the over 40 local density approximation tight-binding (LDA-TB) parameters in our detailed six-band t_{2g} Hamiltonian [Sec. I (VI)] to fit the ARPES bands lying more than 0.15 eV below the Fermi level, achieves nearly perfect agreement *also* for the k_c-dispersion of the quasi-1D bands closer to the Fermi level. This includes agreement with the size and shape of the resonance peak in the upper band—blue in panel (c2)—*without* having modified any of the 17 (a, g, α, γ) parameters I (46) describing the hybridization between the xy and the xz and yz V&C bands, parameters which, we shall see, decisively influence the structure of the metallic $\widetilde{xy}$ bands via the second-order terms (8) and (9) in the two-band Hamiltonian (4).

The resonance peaks are pushed up (down) in the upper (lower) $\widetilde{xy}$ band by the edges of V (C) bands, whose characters

before hybridization with the xy band are 50% *mixed* $|xz;\mathbf{k}\rangle$ and $|xz;\mathbf{k}+\mathbf{c}^*\rangle$ or $|yz;\mathbf{k}\rangle$ and $|yz;\mathbf{k}+\mathbf{c}^*\rangle$; it is therefore not obvious to what extent the character (fatness) of the original xy bands (the red ones in the middle panel of Fig. II 4) near $k_c = \pm 0.75$ or ± 0.25 are retained in the hybridized $\widetilde{xy}$ bands, and, hence, how strong the ARPES intensity should be. The selection rule that the ARPES intensity follows the $|\mathbf{k}\rangle$ character holds also for the two weakly hybridized $\widetilde{xy}$ bands, because—to lowest order—the effect of weak hybridization is to distort the bands. The $|\mathbf{k}\rangle$ character we then compute by expressing the two bands in the $\{\mathbf{k}, \mathbf{k}+\mathbf{c}^*\}$ representation and add to the diagonal elements, $\langle\mathbf{k}|H|\mathbf{k}\rangle$, of the two-band Hamiltonian a few small, equidistant energies. This produces fat bands which include the effects of weak hybridization with the V&C bands [but neglects the relatively small effects of dimerization distortion, $\eta(\boldsymbol{\kappa})$, Eq. II (9)].

We therefore need to compute the $|\mathbf{k}\rangle$ character of the $\widetilde{xy}$ bands. This we do by using the Hamiltonian (4) obtained by downfolding [3] of the V&C blocks of the six-band Hamiltonian I (56) in the $\{\mathbf{k}, \mathbf{k}+\mathbf{c}^*\}$ representation. For simplicity of the formalism, we neglect the mixing between the xz and yz WOs, which is a good approximation near the FS, $|k_b| \approx 0.25$, far from the Y and Z points (see Fig. I 8 or II 1). The derivation of this two-band Hamiltonian will be our first task in the theoretical Sec. II of the present paper.

The two-band Hamiltonian is also the one from which we can best understand the origin of the splitting and perpendicular dispersion of the two metallic bands shown in Fig. 1, including their development with increasing k_b, which is surprisingly nonsymmetric around half filling, $k_b = 0.25$. Having discussed the two bands in great detail in Sec. II B and understood that merely the light-red xy—but *not* the dark-red $\widetilde{xy}$—bands can be described by a 2×2 TB Hamiltonian, we shall, in the final theoretical Sec. II C, present and discuss their constant-energy contours (CECs); the FS in particular.

The second part of this paper, starting from Sec. III, is devoted to the demanding task of using ARPES to determine the FS and its velocities. First, the challenges, issues, and methods are discussed in Sec. III A. The results of the FS and velocity extraction are then shown in Sec. III B. They are compared with the TB theory using the ARPES-refined parameters and are finally presented in Fig. 8.

In theory, the (fine-grained) ARPES intensity from each metallic band is periodic in the double zone ($|\kappa_c| \leqslant 1$) with the intensity from the lower band (outer sheet) dominating in the first zone ($|\kappa_c| \leqslant 0.5$) and the intensity from the upper band (inner sheet) dominating in the second zone ($|\kappa_c| \geqslant 0.5$). Between zone centers (κ_c integer), the origin of the dominating intensity thus switches from one band (sheet) to the other, with the intensities being equal at the zone boundary (see Fig. 5). Since the measured spectra of the sheets possess a finite width in momentum, which is much larger than the splitting of the sheets, we can only detect the center of gravity of the sum of intensities from the occupied bands. By taking this into account, the experimentally obtained FS fits the theoretical one very well. At the zone boundary, we determined an upper bound for the splitting, which is, in that sense, in agreement with the theory, that it is larger than the theoretical value. Comparing the experimentally extracted velocities with the theoretical ones, we reach a similar perfect fit as for the FS. Interestingly, the velocities are generally greater than those for pure LDA by about 15%, as we discuss in detail in Sec. III B 2.

II. THEORETICAL SPLITTING AND PERPENDICULAR DISPERSION OF THE TWO METALLIC BANDS IN THE GAP

A. Hamiltonian for the two metallic bands in the $\{\mathbf{k}, \mathbf{k}+\mathbf{c}^*\}$ representation and of resonance form

We start from the six-band Hamiltonian I (56) in the $\{\mathbf{k}, \mathbf{k}+\mathbf{c}^*\}$ representation:

H	$\lvert xy;\mathbf{k}\rangle$	$\lvert xy;\mathbf{k}+\mathbf{c}^*\rangle$	$\lvert xz;\mathbf{k}\rangle$	$\lvert xz;\mathbf{k}+\mathbf{c}^*\rangle$	$\lvert yz;\mathbf{k}\rangle$	$\lvert yz;\mathbf{k}+\mathbf{c}^*\rangle$
$\langle xy;\mathbf{k}\rvert$	$\tau+t$	iu	$\alpha+a$	$i(\gamma+g)$	$\bar\alpha+\bar a$	$i(\bar\gamma+\bar g)$
$\langle xy;\mathbf{k}+\mathbf{c}^*\rvert$	$-iu$	$\tau-t$	$i(\gamma-g)$	$\alpha-a$	$i(\bar\gamma-\bar g)$	$\bar\alpha-\bar a$
$\langle xz;\mathbf{k}\rvert$	$\alpha+a$	$-i(\gamma-g)$	A	iG	$\lambda+l$	$-i(\mu-m)$
$\langle xz;\mathbf{k}+\mathbf{c}^*\rvert$	$-i(\gamma+g)$	$\alpha-a$	$-iG$	$-A$	$-i(\mu+m)$	$\lambda-l$
$\langle yz;\mathbf{k}\rvert$	$\bar\alpha+\bar a$	$-i(\bar\gamma-\bar g)$	$\lambda+l$	$i(\mu+m)$	$\bar A$	$i\bar G$
$\langle yz;\mathbf{k}+\mathbf{c}^*\rvert$	$-i(\bar\gamma+\bar g)$	$\bar\alpha-\bar a$	$i(\mu-m)$	$\lambda-l$	$-i\bar G$	$-\bar A$

(I (56))

Like in Eq. I (35), the argument $\mathbf{k}$ of the Bloch sums of hopping integrals I (36)–I (40) is omitted for brevity and an overbar, used when switching from an xz to a yz orbital, indicates the mirror operation $k_b \leftrightarrow -k_b$.

1. Six-band Hamiltonian in the V&C subband representation

Since the largest off-diagonal elements I (43)–I (47) are $\bar G$ and G, which gap the yz bands as in Eq. I (29) and the xz bands in the same way, but with k_b substituted by $-k_b$, we now turn to a representation in which the xz-xz and yz-yz blocks are diagonal. This mixed representation is the natural one to use for downfolding these blocks of the six-band Hamiltonian to a two-band Hamiltonian which then describes merely the two $\widetilde{xy}$ bands in the gap and—provided that we neglect the hybridization I (40) between the xz and yz bands—has the simple resonance form (4). As said above, this approximation of using the (m, m')-unhybridized, so-called *pure* xz and yz bands [Sec. I (VI C)] is a good one far from Y and Z, especially near the FS, $|k_b| \approx 0.25$ (Fig. I 8 or II 1). The eigenvalues, $\pm(\bar A^2 + \bar G^2)^{1/2}$, of the yz-yz 2×2 diagonal block

of the six-band Hamiltonian, Eq. I (56), are the yz conduction- and valence-band (C- and V-band) energies I (29), and so are $\pm(A^2+G^2)^{1/2}$ for the xz ^C_V-band energies. The structure of the six bands for $k_b = 0.225$, 0.250, and 0.275 as a function of k_c may be seen on the 3rd line to the left in Fig. 2 and we describe it in Sec. II B.

The orthonormal xz C&V-band orbitals are

$$(|xz_{\rm C}(\mathbf{k})\rangle\ |xz_{\rm V}(\mathbf{k})\rangle) = (|xz;\mathbf{k}\rangle\ |xz;\mathbf{k}+\mathbf{c}^*\rangle) \times \frac{1}{2}\begin{pmatrix} e^{-i\phi}-1 & e^{-i\phi}+1 \\ e^{-i\phi}+1 & e^{-i\phi}-1 \end{pmatrix}, \tag{I (59)}$$

where the xz band-structure phase $\phi(\mathbf{k})$ is that of $-A(\mathbf{k}) - iG(\mathbf{k})$. The $|\mathbf{k}\rangle (= 1 - |\mathbf{k}+\mathbf{c}^*\rangle)$ characters—or fatnesses—of the ^C_V bands are

$$f_{\substack{C\\V}}(\mathbf{k}) = \left|\frac{e^{-i\phi}\mp 1}{2}\right|^2 = \frac{1\mp\cos\phi}{2}, \tag{I (61)}$$

and they are shown on the 3rd line to the right in Fig. 2 in light (dark) blue. While the (C and V) bands are periodic, their fatnesses are periodic in the double zone (see Fig. I 6).

Using the unitary matrix I (59) to transform the six-band Hamiltonian I (56) to the pure-xz representation in which the V&C block is diagonal yields:

H	$\lvert xy;\mathbf{k}\rangle$	$\lvert xy;\mathbf{k}+\mathbf{c}^*\rangle$	$\lvert xz_{\rm C}(\mathbf{k})\rangle$	$\lvert xz_{\rm V}(\mathbf{k})\rangle$
$\langle xy;\mathbf{k}\rvert$	$\tau + t$	iu	cc	cc
$\langle xy;\mathbf{k}+\mathbf{c}^*\rvert$	$-iu$	$\tau - t$	cc	cc
$\langle xz_{\rm C}(\mathbf{k})\rvert$	$(\alpha+a)\frac{e^{i\phi}-1}{2} - i(\gamma+g)\frac{e^{i\phi}+1}{2}$	$(\alpha-a)\frac{e^{i\phi}+1}{2} - i(\gamma-g)\frac{e^{i\phi}-1}{2}$	$\sqrt{A^2+G^2}$	0
$\langle xz_{\rm V}(\mathbf{k})\rvert$	$(\alpha+a)\frac{e^{i\phi}+1}{2} - i(\gamma+g)\frac{e^{i\phi}-1}{2}$	$(\alpha-a)\frac{e^{i\phi}-1}{2} - i(\gamma-g)\frac{e^{i\phi}+1}{2}$	0	$-\sqrt{A^2+G^2}$

(1)

for the first four rows and columns. The last two (yz_C and yz_V) rows and columns obtained by transformation to the pure-yz representation equal those given above for xz_C and xz_V but with k_b substituted by $-k_b$ or A and G substituted by $\bar{A}$ and $\bar{G}$.

2. *Löwdin-downfolded two-band Hamiltonian*

The WOs for the two $\widetilde{xy}$ bands in the gap have much longer range than the xy-WOs shown in Figs. I 5 and I 9, and similarly for the elements in the effective two-band Hamiltonian compared with the range of the Bloch sums in the six-band Hamiltonian. For this reason, we do not perform the downfolding of the xz, XZ, yz, and YZ WOs into the "tails" of the $\widetilde{xy}$ and $\widetilde{XY}$ WOs in real space, but in reciprocal space. Real-space pictures of these downfolded orbitals would be unwieldy and would crucially depend on the position of the energies E of the bands in the gap. For the same reason, tables of hopping integrals would be unwieldy and energy dependent. For the downfolding from six to two narrow bands near the center of the gap, we can use simple, analytical Löwdin [3] rather than numerical (order-N muffin tin orbital) downfolding because the splitting of the two $\widetilde{xy}$ bands is far less than their distance to the C&V-band edges (see the left-hand panels on the 3rd line in Fig. 2). Hence, the explicit dependence of the two-band Hamiltonian (4) on the TB parameters I (43)–I (47) is preserved.

With the hybridization between the xz and yz orbitals neglected, the xz and yz downfoldings are additive:

$$(|\widetilde{xy};E,\mathbf{k}\rangle\ |\widetilde{xy};E,\mathbf{k}+\mathbf{c}^*\rangle) = (|xy;\mathbf{k}\rangle\ |xy;\mathbf{k}+\mathbf{c}^*\rangle) + \delta_{xz;E}(|xy;\mathbf{k}\rangle\ |xy;\mathbf{k}+\mathbf{c}^*\rangle) + \delta_{yz;E}(|xy;\mathbf{k}\rangle\ |xy;\mathbf{k}+\mathbf{c}^*\rangle). \tag{2}$$

Here, the $\delta_{xz;E}$ and $\delta_{yz;E}$ perturbations involve the Green's function for the xz-xz or yz-yz block of the six-band Hamiltonian I (56) times the corresponding xz-xy or yz-xy hybridization matrix. The representation chosen for the xz and yz states to be downfolded (integrated out) matters for the formalism, but *not* for the resulting two-band Hamiltonian. Choosing the pure-m representation (1) in which the xz-xz and the yz-yz blocks of the Hamiltonian are diagonal we get

$$\delta_{xz;E}(|xy;\mathbf{k}\rangle\ |xy;\mathbf{k}+\mathbf{c}^*\rangle) = \frac{|xz_{\rm C}\rangle}{E-\sqrt{A^2+G^2}}(\langle xz_{\rm C}|H|xy;\mathbf{k}\rangle\ \langle xz_{\rm C}|H|xy;\mathbf{k}+\mathbf{c}^*\rangle) + \frac{|xz_{\rm V}\rangle}{E+\sqrt{A^2+G^2}}(\langle xz_{\rm V}|H|xy;\mathbf{k}\rangle\ \langle xz_{\rm V}|H|xy;\mathbf{k}+\mathbf{c}^*\rangle), \tag{3}$$

and similarly for $\delta_{yz;E}$. It is by virtue of this choice that the E dependence of the downfolded orbitals enters solely through the denominators in (3).

In the $\{\widetilde{xy}; E, \mathbf{k}, \mathbf{k}+\mathbf{c}^*\}$ representation (2), the two-band Hamiltonian is finally seen to be

$$\begin{pmatrix} \langle \widetilde{xy}; E, \mathbf{k}|H|\widetilde{xy}; E, \mathbf{k}\rangle & \langle \widetilde{xy}; E, \mathbf{k}|H|\widetilde{xy}; E, \mathbf{k}+\mathbf{c}^*\rangle \\ \text{c.c.} & \langle \widetilde{xy}; E, \mathbf{k}+\mathbf{c}^*|H|\widetilde{xy}; E, \mathbf{k}+\mathbf{c}^*\rangle \end{pmatrix} = \tau(k_b)\begin{pmatrix} 1 & 0 \\ 0 & 1 \end{pmatrix} + \begin{pmatrix} t(\mathbf{k}) & iu(\mathbf{k}) \\ -iu(\mathbf{k}) & -t(\mathbf{k}) \end{pmatrix}$$
$$+ \frac{\Gamma_{\mathrm{C}}(\mathbf{k})}{E - \sqrt{A^2(\mathbf{k}) + G^2(\mathbf{k})}} + \frac{\Gamma_{\mathrm{V}}(\mathbf{k})}{E + \sqrt{A^2(\mathbf{k}) + G^2(\mathbf{k})}} + \frac{\overline{\Gamma}_{\mathrm{C}}(\mathbf{k})}{E - \sqrt{\bar{A}^2(\mathbf{k}) + \bar{G}^2(\mathbf{k})}} + \frac{\overline{\Gamma}_{\mathrm{V}}(\mathbf{k})}{E + \sqrt{\bar{A}^2(\mathbf{k}) + \bar{G}^2(\mathbf{k})}}, \tag{4}$$

with the directly coupled terms on the 1st line and the resonance terms for the coupling via the C&V bands on the 2nd line. The poles at the C&V xz and yz bands, $\pm[A^2(\mathbf{k}) + G^2(\mathbf{k})]^{1/2}$ and $\pm[\bar{A}^2(\mathbf{k}) + \bar{G}^2(\mathbf{k})]^{1/2}$, are numbers while the residues, $\Gamma_C(\mathbf{k})$. $\Gamma_V(\mathbf{k})$, $\overline{\Gamma}_C(\mathbf{k})$, and $\overline{\Gamma}_V(\mathbf{k})$, are 2×2 matrices of the following form for the perturbation by the xz C band:

$$\Gamma_{\mathrm{C}}(\mathbf{k}) = \begin{pmatrix} |\langle xz_{\mathrm{C}}(\mathbf{k})|H|xy; \mathbf{k}\rangle|^2 & \langle xy; \mathbf{k}|H|xz_{\mathrm{C}}(\mathbf{k})\rangle\langle xz_{\mathrm{C}}(\mathbf{k})|H|xy; \mathbf{k}+\mathbf{c}^*\rangle \\ \text{c.c.} & |\langle xz_{\mathrm{C}}(\mathbf{k})|H|xy; \mathbf{k}+\mathbf{c}^*\rangle|^2 \end{pmatrix}, \tag{5}$$

and similarly for the perturbation by the xz V band. Since translation of $\mathbf{k}$ by $\mathbf{c}^*$ yields

$$\widehat{\mathbf{c}^*}\langle \mathbf{k}|\Gamma|\mathbf{k}\rangle = \langle \mathbf{k}+\mathbf{c}^*|\Gamma|\mathbf{k}+\mathbf{c}^*\rangle, \tag{6}$$

the two diagonal elements with $\mathbf{k}$ in the single zone reduce to *one* real-valued function of $\mathbf{k}$, periodic in the double zone. For the purely imaginary off-diagonal element:

$$\widehat{\mathbf{c}^*}\langle \mathbf{k}|\Gamma|\mathbf{k}+\mathbf{c}^*\rangle = \langle \mathbf{k}+\mathbf{c}^*|\Gamma|\mathbf{k}\rangle = \langle \mathbf{k}|\Gamma|\mathbf{k}+\mathbf{c}^*\rangle^* = -\langle \mathbf{k}|\Gamma|\mathbf{k}+\mathbf{c}^*\rangle, \tag{7}$$

i.e., it is an antiperiodic function of $\mathbf{k}$ in the single zone.

The elements of the matrix (5) are given by those of Eq. (1) in terms of the xz-band phase $\phi(\mathbf{k})$ [I (60)] and the Bloch sums of the xy-xz intra- and inter-ribbon hopping integrals $\alpha \pm a$ and $\gamma \pm g$ [I (39)], and may be expressed as

$$\langle \mathbf{k}|\Gamma_{\substack{C\\V}}(\mathbf{k})|\mathbf{k}\rangle = |\langle xz_{\substack{C\\V}}(\mathbf{k})|H|xy; \mathbf{k}\rangle|^2 = \left[(\alpha+a)f_{\substack{C\\V}} \mp (\gamma+g)\frac{\sin\phi}{2}\right]^2 + \left[(\gamma+g)f_{\substack{V\\C}} \mp (\alpha+a)\frac{\sin\phi}{2}\right]^2 \tag{8}$$

for the diagonal elements, and as

$$\langle \mathbf{k}|\Gamma_{\substack{C\\V}}(\mathbf{k})|\mathbf{k}+\mathbf{c}^*\rangle = \langle xy; \mathbf{k}|H|xz_{\substack{C\\V}}(\mathbf{k})\rangle\langle xz_{\substack{C\\V}}(\mathbf{k})|H|xy; \mathbf{k}+\mathbf{c}^*\rangle$$
$$= i\left[-(\alpha+a)(\gamma-g)f_{\substack{C\\V}} + (\gamma+g)(\alpha-a)f_{\substack{V\\C}} \pm \left((\alpha+a)(\alpha-a) + (\gamma+g)(\gamma-g)\frac{\sin\phi}{2}\right)\right] \tag{9}$$

for the off-diagonal elements, which are purely imaginary. They are shown on the 4th line of Fig. 2 as functions of k_c for $k_b = 0.225$, 0.250, and 0.275 and will be discussed in Sec. II B 5. On the 5th line, we show the xy-xz intra and inter-ribbon hopping integrals: to the left $\alpha + a$ in purple and $\alpha - a$ in gray, and to the right $\gamma + g$ in turquoise and $\gamma - g$ in gray. These Bloch sums are periodic in the double zone and each gray Bloch sum equals the colored one inside the same frame, but translated by $\mathbf{c}^*$. This follows from Eqs. I (41) and (42). Together with the $|\mathbf{k}\rangle$ characters of the C and V bands, f_C and f_V, in respectively light and dark blue on the 3rd line to the right, $\frac{1}{2}\sin\phi$ is shown in gray.

The residues for the perturbations by the yz C&V bands are respectively $\overline{\Gamma}_C(\mathbf{k})$ and $\overline{\Gamma}_V(\mathbf{k})$ with the overbar indicating the mirror operation $k_b \leftrightarrow -k_b$.

E is the energy of the $\widetilde{xy}$ state that we are seeking, i.e., the upper or lower eigenvalue of the two-band Hamiltonian (4), and should therefore be found self-consistently. For states deep inside the gap, we may substitute E by $\tau(k_b)$ from Eq. I (36) because the splitting of the two $\widetilde{xy}$ bands is far less than half the gap. Note that E is with respect to the center of the gap and that it enters the two-band Hamiltonian (4) only through the denominators of the four resonance terms. Keeping E as a free parameter therefore provides insight to study how the perpendicular dispersion of the $\widetilde{xy}$ bands depend on their placement in the gap and on the $\mathbf{k}$ dependence of the four residues.

The simplest way to understand the energy dependence of a Löwdin-downfolded Hamiltonian $\widetilde{H}(E)$ is to consider downfolding of a 2×2 Hamiltonian H: Its exact E eigenvalues are the roots of the secular determinant $|H - E1| = (H_{11} - E)(H_{22} - E) - |H_{12}|^2$, which satisfy $E = H_{11} + |H_{12}|^2/(E - H_{22}) \equiv \widetilde{H}(E)$, showing that $\widetilde{H}(H_{11})$ is the well-known second-order estimate of the eigenvalue closest to H_{11} and that $\widetilde{H}(E)$ has a pole at the energy H_{22}. It should now be obvious that the six-band Hamiltonian (1) can be downfolded to a two-band Hamiltonian with the form (4).

B. Origin of the splitting and perpendicular dispersion

Having derived a Hamiltonian (4) for the two metallic $\widetilde{xy}$ bands in the gap (Fig. 1) consisting of TB *plus resonance* terms, we now take up the thread and trace the nontrivial features of the bands back to the Bloch sums I (36) and I (37), $\tau(k_b)$, $t(\mathbf{k})$, and $u(\mathbf{k})$, of the xy-xy hopping integrals, to the Bloch sums I (38), $A(k_c \mp k_b)$ and $G(k_c \mp k_b)$, of the xz-xz or yz-yz hopping integrals, and to the Bloch sums I (39), $\alpha(\mathbf{k}) \pm a(\mathbf{k})$ and $\gamma(\mathbf{k}) \pm g(\mathbf{k})$, of the xy-xz hopping integrals.

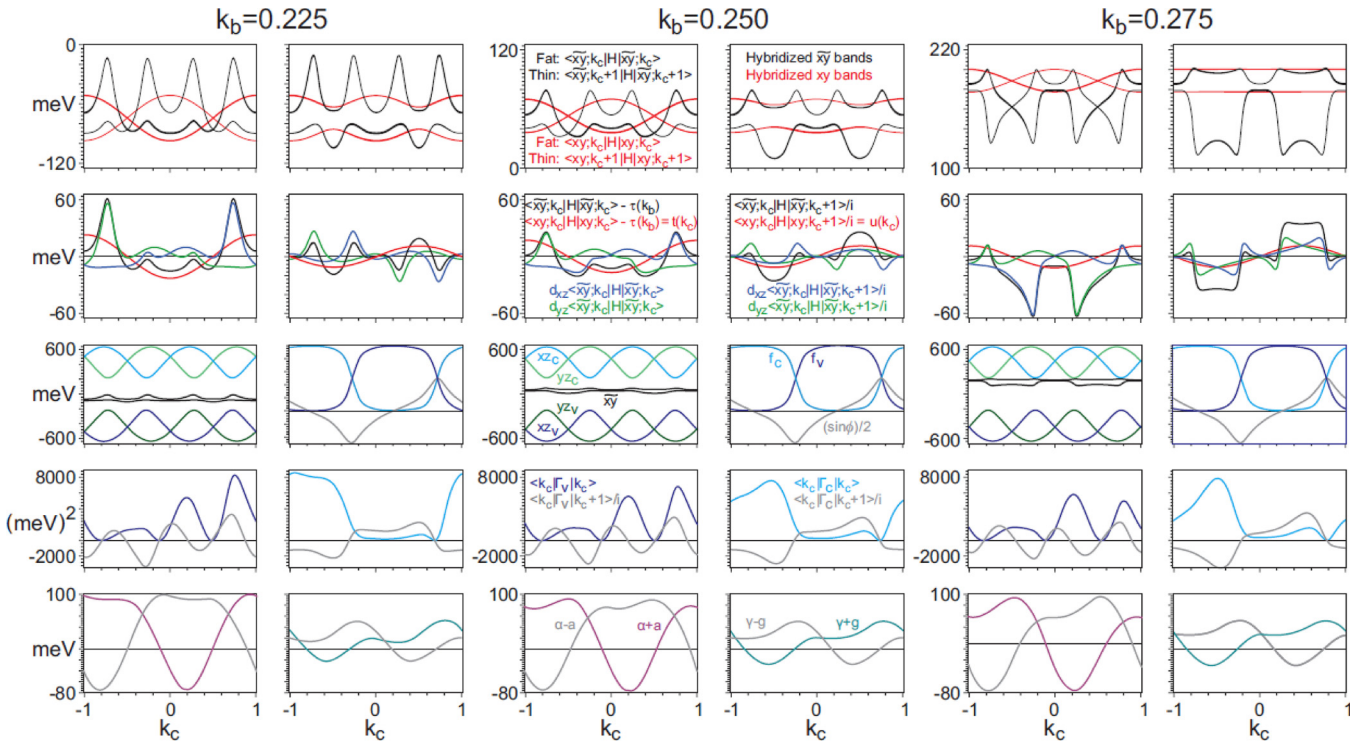

FIG. 2. The following caption is for each of the three k_b panels: (1st line) The two metallic xy (red) and $\widetilde{xy}$ (black) bands, decorated with their $|\mathbf{k}\rangle$ character, as fct.s of k_c in the double zone. $(\mathbf{k}, \mathbf{k}+\mathbf{c}^*)$ unhybridized (left) and hybridized (right). The latter are as in Fig. 1 but extended to the double zone. As functions of (k_b, k_c), the six bands were shown on a 2 eV scale in Fig. I 4 and the two metallic bands are shown on a 0.3 eV scale in Figs. 3(a)–3(c). (2nd line) Diagonal $\langle\widetilde{xy};\mathbf{k}|H|\widetilde{xy};\mathbf{k}\rangle - \tau(k_b)$ (left), and off-diagonal $\langle\widetilde{xy};\mathbf{k}|H|\widetilde{xy};\mathbf{k}+\mathbf{c}^*\rangle/i$ (right), elements of the two-band Hamiltonian (4). In black, the sum of the contributions from the direct, inter-ribbon xy-XY hops (red) and from the indirect hops via the xz (blue) and yz (green) valence (V) and conduction (C) bands. [Not shown are the $xy(\mathbf{k}+\mathbf{c}^*)$ and $\widetilde{xy}(\mathbf{k}+\mathbf{c}^*)$ bands minus $\tau(k_b)$ in thin black]. (3rd line, left) The black $\widetilde{xy}$ bands in the gap between the blue xz and green yz V (dark) and C (light) bands; the hybridizations of the two latter with the xy bands were neglected, i.e., $\varepsilon_{xz} = \mp(A^2+G^2)^{1/2}$, but not vice versa. (3rd line, right) Light (dark) blue: the probability that at $\mathbf{k}$, the $|xz;\mathbf{k}\rangle$ character is in the C (V) band is $f_{\substack{\mathrm{C}\\\mathrm{V}}} \equiv (1 \mp \cos\phi)/2$, Eq. I (61). Gray: $(\sin\phi)/2$. (4th line) Diagonal (blue) and off-diagonal (gray) matrix elements, (8) and (9), in meV^2 of the residue for the perturbation of the two-band Hamiltonian via the xz V band (left) or C band (right). (5th line, left) Bloch sums of xy-xz hopping integrals I (39): $\alpha + a$(purple), $\alpha - a$ (gray); (right) $\gamma + g$ (turquoise), $\gamma - g$ (gray). These four Bloch sums are periodic in the double zone and each gray Bloch sum equals the colored one inside the same frame, but translated by $\mathbf{c}^*$. Energies are in meV with respect to the center of the gap. The ARPES-refined parameter values were used. E in the resonance terms was approximated by $\tau(k_b)$. See Secs. I (VI) and II A.

This is a long route and the essence may be extracted from the synthesis in Sec. II B 7.

We start by extending Fig. 1 from the irreducible ($0 \leqslant k_c \leqslant 0.5$) to the double ($-1 < k_c \leqslant 1$) zone in which all Bloch sums are periodic (the Greek- and Latin-lettered Bloch sums are periodic in respectively the single and the double zone). This is done in Fig. 2 on the top line to the right (the figure to the left will be described in the last paragraph of this section), in each of three panels, for $k_b = 0.225$, 0.250, and 0.275, i.e., along the brown, red, and olive dot-dashed lines in Fig. I 8 or II 1. For clarity, the color of the $\widetilde{xy}$ bands has been changed from dark-red to black in Fig. 2.

Upon increasing k_b from 0.225 to 0.275, we see the $\widetilde{xy}$ bands develop from having strong upward-pointing peaks in the upper band near $k_c = \pm 0.75$ and ± 0.25, plus small downward bulges in the lower band around $k_c = \pm 0.5$, over having reduced peaks and increased bulges—and thus minimal total width—near midgap, to having large downward-pointing peaks connected pairwise by large bulges in the lower band, plus reminiscences of the upward-pointing peaks in the upper band. This development is far from symmetric around the midgap energy ($\equiv 0$), despite the fact that the V and C bands on either side of the direct gap have the same character, apart from being respectively xz-XZ (or yz-YZ) bonding and antibonding. In the present section we show in didactic detail that the origin lies in the complicated bi-products (5) forming the residues $\Gamma(\mathbf{k})$ of the matrix elements for the resonant couplings.

On lines 2–5 in Fig. 2, we identify and analyze the individual contributions from the direct xy-xy hops (red) and the indirect hops via the xz (blue) and yz (green) V&C bands to the diagonal and off-diagonal elements $\langle\widetilde{xy};\mathbf{k}|H|\widetilde{xy};\mathbf{k}\rangle$ and $\langle\widetilde{xy};\mathbf{k}|H|\widetilde{xy};\mathbf{k}+\mathbf{c}^*\rangle$, of the two-band Hamiltonian (4). We end on line 5 with $\alpha(\mathbf{k}) \pm a(\mathbf{k})$ in purple (gray) and $\gamma(\mathbf{k}) \pm g(\mathbf{k})$ in turquoise (gray).

For simplicity in Fig. 2, we have substituted E in the denominators of the resonance terms (4) by $\tau(k_b)$ and shall use a notation in which we drop this argument from,

e.g., $\langle\widetilde{xy};\tau(k_b),\mathbf{k}|\,H\,|\widetilde{xy};\tau(k_b),\mathbf{k}+\mathbf{c}^*\rangle$. This approximation slightly enhances the peak features, as may be seen by comparison of Figs. 1 and 2.

The bands—but not their $|\mathbf{k}\rangle$ decoration (extra fatness)—have the proper single-zone period 1 in k_c. Where one band is fat and the other not, those bands have respectively pure $|\mathbf{k}\rangle$ and pure $|\mathbf{k}+\mathbf{c}^*\rangle$ character. This is the case for integer values of k_c, whereas for half-integer values, the two bands are of 50% mixed character.

To the left on the 1st line, we show in respectively fat and thin lines the unhybridized $\widetilde{xy}(\mathbf{k})$ and $\widetilde{xy}(\mathbf{k}+\mathbf{c}^*)$ bands. These are the diagonal elements $\langle\widetilde{xy};\mathbf{k}|H|\widetilde{xy};\mathbf{k}\rangle$ and $\langle\widetilde{xy};\mathbf{k}+\mathbf{c}^*|H|\widetilde{xy};\mathbf{k}+\mathbf{c}^*\rangle$ of the two-band Hamiltonian (4) and have the double-zone period 2 in k_c.

1. Peak, bulge, and contact features

The *primary feature* of the $\widetilde{xy}$ bands in the gap, the *resonance peaks*, originate from either an xz-band edge, which runs along a blue YZY′ line in Fig. I 8 and II 1, or from a yz-band edge, which runs along a green YZY′ line in the same figure, and are therefore located at the crossings between such a line and the two red $\widetilde{xy}$-band CECs seen in the uppermost panels of Fig. II 10(b). In the CECs, the resonance peaks appear as *notches*. With reference to the bands for fixed values of k_b in Fig. 1, a resonance peak is located where a band edge crosses the appropriate constant k_b line (dot-dashed in Fig. I 8 and II 1). The resonance features are therefore well separated in k_c as seen in Fig. 2 on the 1st line to the right.

From the fatnesses of the bands we see that the resonance peaks have almost pure $|\widetilde{xy};\mathbf{k}\rangle$ or $|\widetilde{xy};\mathbf{k}+\mathbf{c}^*\rangle$ character, although the V&C-band edges have ≈50% mixed $|xz;\mathbf{k}\rangle$ and $|xz;\mathbf{k}+\mathbf{c}^*\rangle$ (or $|yz;\mathbf{k}\rangle$ and $|yz;\mathbf{k}+\mathbf{c}^*\rangle$) characteristics, as we saw along ΛW ($k_c=\frac{1}{4}$) and Λ′W′ ($k_c=\frac{3}{4}$) in Figs. II 11(d) and II 11(e). The strong $|\mathbf{k}\rangle$ character is what enabled us, in Sec. IV B of paper II [2], to detect with ARPES the large peak in the upper $\widetilde{xy}$ band from the resonance with the blue xz valence band at $\mathbf{k}=(0.225,0.725)$, mirrored ("symmetrized") around $k_c=0.5$ to $(0.225,0.275)$. That the lower $\widetilde{xy}$ band merely exhibits a shoulder at $(0.225,0.725)$ will be explained later, at the beginning of Sec. II B 5.

The understanding is quite different for the *secondary feature*, seen around the BZ boundaries ($k_c=\pm0.5$) on the 1st line in Fig. 2 to the right (but absent to the left). This feature consists of a *bulge* in the lower band and the concomitant filling-in of the valleys between the neighboring resonance peaks repelled by the xz and yz V or C bands, whichever is closer in energy. These neighboring resonance peaks are therefore in the upper $\widetilde{xy}$ band when $k_b=0.225$ and 0.250 and in the lower $\widetilde{xy}$ band when $k_b=0.275$. The bulge is caused by the hybridization between the $\widetilde{xy}(\mathbf{k})$ and $\widetilde{xy}(\mathbf{k}+\mathbf{c}^*)$ bands—displayed to the left—which cross at $k_c=\pm0.5$ and split by $\pm|\langle\widetilde{xy};\mathbf{k}|H|\widetilde{xy};\mathbf{k}+\mathbf{c}^*\rangle|$. The latter, off-diagonal matrix element of the two-band Hamiltonian (4) is shown in black on the 2nd line to the right. This element is seen to attain its largest absolute value near $k_c=\pm0.5$ and, here, to have equal contributions from the indirect hops via the xz (blue) and yz (green) bands, and to be amplified by the direct xy-xy (red) contribution. To the left, and in the same colors, are shown the diagonal element $\langle\widetilde{xy};\mathbf{k}|H|\widetilde{xy};\mathbf{k}\rangle$ and its three contributions.

Also the *third* characteristic *feature* of the $\widetilde{xy}$ bands, the *near contact* between the two bands—and in particular between their CECs [Fig. 3(d)]—on the ΓY and Γ′Y′ lines ($k_c=$ integer), is connected with the hybridization between the $\widetilde{xy}(\mathbf{k})$ and $\widetilde{xy}(\mathbf{k}+\mathbf{c}^*)$ bands, albeit with its zero rather than its maximum (Fig. 2, black curve on the 2nd line to the right). In ARPES [Fig. II 14(c2)], as well as in previous calculations [4], an apparent crossing on the ΓY line ($k_c=0$) was noted and a TB description attempted [5]. With our improved resolution, this peculiarity is now seen [Fig. 3(d)] as a splitting between the two CECs, which along ΓY is anomalously small[2] and even *de*creases with energy. This is in contrast with the relatively large splitting along ZC ($k_c=1/2+$ integer) which is caused by $(\mathbf{k},\mathbf{k}+\mathbf{c}^*)$ hybridization and increases with energy. The splitting at integer k_c is even *smaller* than that of the directly coupled, red bands. This is simple to understand: First of all, the splitting, $2t(\mathbf{k})=8(t_1\cos\pi k_b+t_2\cos3\pi k_b)$, of the red bands decreases from 46 meV for $k_b=0.225$ to 24 meV for $k_b=0.275$. Second, along ΓY ($k_c=0$) the pure $xy(\mathbf{k})$, $xz(\mathbf{k})$, and $yz(\mathbf{k})$ bands are all bonding between ribbons while the $xy(\mathbf{k}+\mathbf{c}^*)$, $xz(\mathbf{k}+\mathbf{c}^*)$, and $yz(\mathbf{k}+\mathbf{c}^*)$ bands are all antibonding [see Fig. I 6]. Since both xy bands in the gap lie above the $xz(\mathbf{k})$ and $yz(\mathbf{k})$ bands, but below the $xz(\mathbf{k}+\mathbf{c}^*)$ and $yz(\mathbf{k}+\mathbf{c}^*)$ bands, the valence bands will push the bonding $xy(\mathbf{k})$ band up, and the conduction bands will push the antibonding $xy(\mathbf{k}+\mathbf{c}^*)$ band down in energy. Hence, the hybridization with the xz and yz V&C bands will *diminish* the separation between the xy bands.[3]

It is remarkable that, in a region around $k_c=$ integer, the lower $\widetilde{xy}$ band runs parallel to the red xy band and that the k_c region over which this happens, as well as the distance above the xy band, decreases with increasing k_b.

We emphasize that neither of the three characteristic features of the two metallic bands in the gap can be described by merely a 2×2 TB Hamiltonian, but need the resonance terms. The three characteristic features are seen as functions of (k_b,k_c) on the left-hand side of Fig. 3 in Sec. II C, to which we shall return.

2. Directly coupled terms

We now systematically identify the different terms of the two-band Hamiltonian (4).

Its first term, the energy $\tau(k_b)$ of the two degenerate 1D intraribbon xy bands, is included only on the 1st line of Fig. 2, where it is the average of the two red, directly coupled xy bands, $xy(\mathbf{k})$ and $xy(\mathbf{k}+\mathbf{c}^*)$ to the left, or of the $(\mathbf{k},\mathbf{k}+\mathbf{c}^*)$-hybridized bands to the right. This average is independent of k_c. On the 2nd line to the left, $\tau(k_b)$ is neither included in the red, directly coupled $xy(\mathbf{k})$ band, nor in the black, directly plus indirectly coupled $\widetilde{xy}(\mathbf{k})$ band.

The second term in Eq. (4) is the xy block of the six-band Hamiltonian I (56) and it gives the perpendicular dispersions

[2]Including the xz-yz hybridization, i.e., the (λ,l,μ,m) hopping integrals, as was done in Figs. I 14(c2) and 3(d) but was neglected in the two-band Hamiltonian and, hence, in Figs. 2 and 1, decreases the splitting between the $\widetilde{xy}$ bands for integer k_c by a factor ≈2.

[3]The result along Γ′Y′ ($k_c=\pm1$) is of course the same although, there, the $|\mathbf{k}\rangle$ bands are antibonding and the $|\mathbf{k}+\mathbf{c}^*\rangle$ bands bonding.

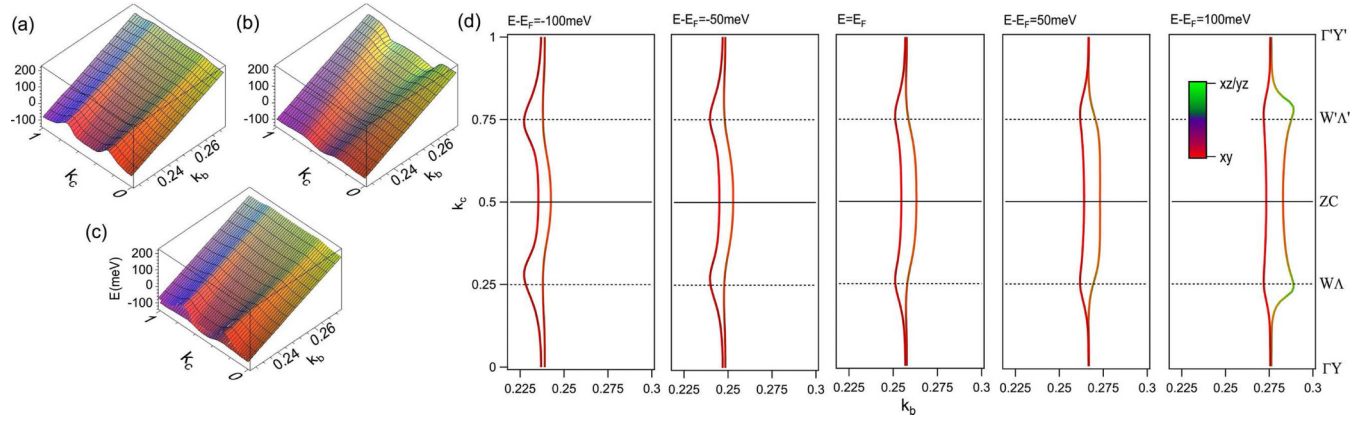

FIG. 3. (a)–(c) The two $\widetilde{xy}$ quasi-1D bands in the gap for the six-band Hamiltonian I (56) with the ARPES-refined parameter values I (43)–I (47). The **k**-space region considered is the stripe ±10% around k_{Fb} in the upper half of the 1st and the lower half of the 2nd BZ, $0 \leqslant k_c \leqslant 1$. The energies of (a) the upper, (b) the lower, and (c) both metallic bands, relative to the center of the gap, defined as 0. $E_F = 75$ meV above the center. (d) CECs calculated by tracing the roots of the secular determinant $|H(k_b, k_c) - E|$. The colors indicate the orbital characters of the bands. The notches in the inner sheet point to Z and those in the outer sheet to Y and Y′ (see Figs. 1 and 10 in paper II [2]). The CECs have been *compressed* by a factor 3.3 along k_c in order to make their warping visible. The ratio between the warping $\delta k_{i\,Fb}$ of each (inner or outer) FS sheet and $k_{Fb} \approx 0.25$ is ≈0.02. This is ≈5 times more than without the resonant coupling to the V&C bands (see red bands for $k_b = 0.25$ in Figs. 1 and 2).

and splitting of the red xy bands shown on the 1st line in Fig. 2. The corresponding diagonal and off-diagonal matrix elements, $t(\mathbf{k})$ and $iu(\mathbf{k})$, are the Bloch sums of respectively the average xy-XY hoppings and their dimerizations. They are given in Eq. I (37) and are shown in red on the 2nd line to, respectively, the left and the right. These Bloch sums of direct hoppings are seen to depend little on k_b in the ±10% interval around k_F.

Also the TB model [5] upon which current Tomonaga—Luttinger-liquid (TLL) theories [6,7] are based, includes first- and second-nearest-neighbor terms. But in the attempt to fit the peak, bulk, and band-crossing features of the LDA FS [4] without recognizing their resonant nature, the resulting TB model had an unphysical form (containing, e.g., $\sin \pi k_c$ and $\sin 2\pi k_c$ terms) and, as a consequence, its parameter values are incompatible with ours. That the magnitude of its FS warping is several times ours is partly because the stoichiometry was taken to be $Li_{0.90}$ rather than $Li_{1.02}$.

3. Symmetries

The red directly coupled and the black directly plus indirectly coupled $|\mathbf{k}\rangle$ bands shown to the left on the 2nd line are even around k_c = integer. The red and black matrix elements shown to the right couple each of these bands to itself after a translation of k_c by one. These off-diagonal elements, divided by i, are odd around k_c = integer and even around $k_c = \pm 0.5$. The indirect couplings alone, i.e., the perturbations of the $\widetilde{xy}$-band Hamiltonian by the xz or yz V&C bands, are shown in, respectively, blue and green. They are related to each other by a sign change[II8] of k_b, and those blue and red curves to the left (right) are related to each other by a mirror (antimirror) operation around k_c = integer. Moreover, each of the blue and green curves to the right change sign upon k_c translation by one, i.e., they are antiperiodic, Eq. (7).

4. Indirectly coupled terms; role of the denominators

The indirect couplings via the xz and yz bands are additive and given by respectively the third and fourth and the fifth and sixth terms in expression (4), provided that the hybridization between the xz and yz bands is neglected.[2] The perturbations via the xz and yz bands have been subdivided into V and C bands whereby each of them takes the form of a single resonance (pole) with the denominator being the distance between the narrow $\widetilde{xy}$ band and one of the four xz or yz V or C bands. The energy of the former is $E[\sim\tau(k_b)]$, the energy of an yz band is given by expression I (29), and that of an xz band by the same expression with k_b substituted by $-k_b$. While each denominator is a single-periodic scalar function of **k**, each nominator (residue) is a double-periodic 2 × 2 matrix function given by Eqs. (5)–(9).

From now on, we shall take advantage of the symmetries mentioned in the previous Sec. II B 3 between the blue xz and the green yz perturbations of the two-band Hamiltonian to consider merely the blue xz perturbation, which we shall trace back from the 2nd line in Fig. 2 to the Bloch sums A and G (of respectively the symmetric and asymmetric xz-xz integrals for hopping inside and outside a biribbon), giving the xz C&V-band energies to the left and their characters, f_C, to the right on the 3rd line, and to the Bloch sums of the integrals for hopping between the xy and xz WOs on the 5th line.

The most important factor influencing the shapes of the diagonal and off-diagonal matrix elements shown in blue on the 2nd line to the left and the right, and given by the third and fourth terms in Eq. (4), is their common energy denominator. This is the distance seen on the 3rd line to the left between the $\widetilde{xy}$ bands in black and the xz V or C bands in, respectively, dark and light blue. Also shown are the yz V and C bands in, respectively, dark and light green. The edges, $\mp 2|G_1|$, of the xz bands (blue in Fig. I 8 and II 1) are along $k_c = k_b \mp 1/2 + 2n$, which for the three chosen values of k_b, and for k_c in the

$(-1|1)$ double-zone are at $k_c \approx -0.25$ and 0.75. This is where the xz-band edges may cause resonance peaks in the $\widetilde{xy}$ bands. The $|\mathbf{k}\rangle$ characters of the xz V and C bands, f_V and f_C, are given by respectively the dark- and light-blue curves to the right on the 3rd line in Fig. 2.

When $k_b = 0.225$, there is a large peak in the $|\mathbf{k}+\mathbf{c}^*\rangle$ unhybridized $\widetilde{xy}(\mathbf{k})$ band on the 1st line to the left near 0.75 and a small one near -0.25. On the 2nd line, both peaks are blue and point upward, i.e., are caused by repulsion from the xz valence band. Their sizes decrease strongly as—with k_b increasing—the $\widetilde{xy}$ bands move upward, away from the valence band. For $k_b = 0.250$, the peaks can still be seen in the unhybridized $\widetilde{xy}(\mathbf{k})$ bands, as well as in the fully hybridized $\widetilde{xy}$ band on the 1st line to the right. But for $k_b = 0.275$, when the upper $\widetilde{xy}$ band is touching the bottom of the C-band edge, only the peak from the xz V-band resonance near 0.75 has survived. The small peak near -0.25 has been overpowered by a large, downward pointing C-band resonance, shaped like a *canine tooth*. Going back to $k_b = 0.250$, this tooth is reduced to a "hole" on the low-k_c side of the small, blue V-band peak near $k_c = -0.25$.

The contribution from the xz V&C bands to the hybridization between the $\widetilde{xy}(\mathbf{k})$ and $\widetilde{xy}(\mathbf{k}+\mathbf{c}^*)$ bands is shown in blue (and divided by i) on the 2nd line to the right. Whereas the diagonal element (8) of the residue matrix (5) is never negative, its $(\mathbf{k}, \mathbf{k}+\mathbf{c}^*)$-mixing off-diagonal elements (9) are purely imaginary and antiperiodic, i.e., they change sign upon translation of k_c by one. For $k_b = 0.225$ the blue peak pointing downward near 0.75 is similar to that of the diagonal element pointing upward, but its magnitude is reduced by roughly a factor of two. For k_b increasing, this peak decreases further and it gets superposed by the growing antiperiodic canine-tooth structure. At the zone boundaries (ZBs), $k_c = \pm 0.5$, and the $\widetilde{xy}(\mathbf{k})$ and $\widetilde{xy}(\mathbf{k}+\mathbf{c}^*)$ bands are degenerate but get split by $\pm$ the numerical value of the off-diagonal element of the two-band Hamiltonian (4), which is seen to increase strongly with k_b. The reason is—as we shall see below—that the contribution from the V band nearly vanishes at the zone boundaries. The uncompensated repulsion from the C band is then what causes the development of the bulge in the lower $\widetilde{xy}$ band.

The V band thus causes peaks in the upper $\widetilde{xy}$ band, and the C band causes merging canine teeth plus ZB-centered bulges in the lower $\widetilde{xy}$ band. The peaks and the teeth are resonance features occurring where the FS, $|k_b| \approx 1/4$, crosses between the edges, $|k_c \pm k_b| = 1/2$, of xz- and yz-like V&C bands.

5. *Indirectly coupled terms; role of the residues*

The sign of a resonance term is that of its denominator, i.e., it is *repulsive*. As a consequence, *if* the Hamiltonian minus $\tau(k_b)$ is dominated by *one* of the resonance terms, e.g., due to a small denominator, that term will repel *one* of the two xy bands, and leave the other band unperturbed. Examples are seen on the 1st line to the right in Fig. 2: Where a resonance peak exists in one of the $\widetilde{xy}$ bands, there is merely a tiny peak or shoulder in the other band. Taking, first, the resonance peak as the one caused by the blue xz valence band near $k_c = 0.75$ for $k_b = 0.225$ or 0.250, the resonance terms parts relevant for the blue δ_{xz} perturbation on the 2nd line to the left,

$$\frac{\langle \mathbf{k}|\Gamma_V|\mathbf{k}\rangle}{\tau(k_b) + \sqrt{A^2(\mathbf{k}) + G^2(\mathbf{k})}}$$

and

$$\frac{\langle \mathbf{k}+c^*|\Gamma_V|\mathbf{k}+c^*\rangle}{\tau(k_b) + \sqrt{A^2(\mathbf{k}) + G^2(\mathbf{k})}},$$

are those near $k_c = 0.75$ and -0.25. The closeness of the black and blue curves confirms that the Hamiltonian is, in fact, dominated by this *one* resonance term. Next, we go to $k_b = 0.275$ where the $\widetilde{xy}$ bands are located just below the bottom of the C bands. The peak in the upper band caused by the repulsion from the V-band edge can still be seen on the top line to the right near $k_c = 0.75$, but the nearby C-band edge repels the lower band much further. In fact, it is now the upper band which is the flatter and has an energy near the upper red, pure xy band. The closeness of the black and blue curves on the 2nd line to the left confirms that the Hamiltonian is dominated by the xz-band resonances, with a minor, peak-shaped contribution from the V band near $k_c = 0.75$ and a major, contribution with the shape of a canine tooth from the C band near $k_c = -0.25$. This behavior is also clearly seen in the band structures, Figs. II 12 and II 14, along the ZY and WΛ lines as was described in Sec. IV of paper II [2]. This could be another reason for the "nonlinearity" seen in Fig. 7.

The residues $\Gamma(\mathbf{k})$ of the four resonance terms in expression (4) are 2×2 matrices (5) with diagonal elements forming a real-valued, non-negative function of $\mathbf{k}$ which is periodic in the double zone (6) and imaginary off-diagonal elements forming an antiperiodic function of $\mathbf{k}$ in the single zone (7). These properties are clearly exhibited by the plots of expressions (8) and (9) on the 4th line of Fig. 2 showing $\Gamma_C(\mathbf{k})$ on the right-hand sides with the diagonal element $\langle \mathbf{k}|\Gamma_C|\mathbf{k}\rangle$ in light blue and the off-diagonal element $\langle \mathbf{k}|\Gamma_C|\mathbf{k}+\mathbf{c}^*\rangle/i$ in gray. Similarly on the left-hand sides: $\Gamma_V(\mathbf{k})$ with the diagonal element $\langle \mathbf{k}|\Gamma_V|\mathbf{k}\rangle$ in dark blue and the off-diagonal element $\langle \mathbf{k}|\Gamma_V|\mathbf{k}+\mathbf{c}^*\rangle/i$ in gray. Whereas the light blue conduction band residue follows $|\mathbf{k}\rangle$ character of the conduction band, f_C (3rd line to the right), as expected, the dark blue valence-band residue drops to zero near $k_c = 0.5$, which is in the middle of the region where the $|\mathbf{k}\rangle$ character of the valence band dominates, and the same happens near -0.1. Expression (8) together with the plots of $\alpha \pm a$ and $\gamma \pm g$ on the 5th line show that the reason for the unexpected behavior of Γ_V is the U shape with two zeros of $\alpha(\mathbf{k}) + a(\mathbf{k})$. The zero of Γ_V near -0.85 is caused by the zero of $\gamma(\mathbf{k}) + g(\mathbf{k})$ shown in turquoise on the bottom line to the right.

The peaks due to resonances with the xz bands occur near the xz-band edges. Exactly at the edges, $f_C = f_V = 1/2$ and $\sin\phi = \pm 1$. The $\mathbf{k}$-conserving part of the residues therefore takes the values

$$\langle \mathbf{k}|\Gamma_{\substack{C\\V}}|\mathbf{k}\rangle = \tfrac{1}{2}[(\alpha + a) \pm (\gamma + g)\sin\phi]^2. \qquad (10)$$

The magnitudes and signs of $\alpha + \alpha$ and $\gamma + g$ shown in respectively purple and turquoise on the 5th line, cause the Γ_V coupling at the $k_c = 0.75$ edge (where $\sin\phi = -1$) and the Γ_C coupling at the $k_c = -0.25$ edge (where $\sin\phi = 1$) to be much stronger than the two others, i.e., than the Γ_V coupling

at -0.25 and the Γ_C coupling at 0.75, which even has a "hole" here. This is exactly the behavior of the blue peaks seen on the 2nd line to the left.

We finally come to the gray, off-diagonal elements, $\langle \mathbf{k}|\Gamma|\mathbf{k}+\mathbf{c}^*\rangle$, on the 4th line. They are—roughly speaking—antiperiodic (7) versions of the double-periodic blue, diagonal elements. The reason why the gray $\langle \mathbf{k}|\Gamma_V|\mathbf{k}+\mathbf{c}^*\rangle$ to the left is far more wiggly than the gray $\langle \mathbf{k}|\Gamma_C|\mathbf{k}+\mathbf{c}^*\rangle$ to the right, is that not only does the former possess the two "extra" zeros from $\alpha + a$ near -0.1 and 0.5, as well as the one from $\gamma + g$ at -0.85, but also those translated by 1, i.e., those near -0.5, 0.9, and 0.15.

These very different k_c dependencies seen on the 4th line of the blue $\langle \mathbf{k}|\Gamma_C|\mathbf{k}\rangle$ and $\langle \mathbf{k}|\Gamma_V|\mathbf{k}\rangle$ curves, and of the gray $\langle \mathbf{k}|\Gamma_C|\mathbf{k}+\mathbf{c}^*\rangle$ and $\langle \mathbf{k}|\Gamma_V|\mathbf{k}+\mathbf{c}^*\rangle$ curves, i.e., of the conduction- and valence-band residues, are the causes of the strong asymmetry of the perpendicular dispersion and splitting of the metallic bands around the center of the gap.

6. xy-xz and xy-yz hopping integrals

The purple $\alpha \pm a$ and turquoise $\gamma \pm g$ Bloch sums I (39) shown on the bottom line are determined by the hopping integrals, a_n, g_n, α_n, and γ_n, computed as matrix elements I (9) of the LDA Hamiltonian between nth-nearest-neighbor xy and xz (or XZ) WOs (see Fig. I 9) with the results given in Eq. I (46). Specifically, the integrals for hopping between xy and XZ WOs on *different* sublattices are $a_n \pm g_n$. Here, a_1 is the average of and g_1 half the difference between the integrals for hopping from xy at the origin to XZ on the neighboring ribbon, inside or outside the same biribbon, i.e., to XZ at respectively $-0.012\mathbf{a} - 0.5\mathbf{b}{+}0.467\mathbf{c}$ and $-(0.012\mathbf{a}{-}0.5\mathbf{b}{+}0.533\mathbf{c})$; similarly for a_1' and g_1', except that the XZ orbital is translated by $\mathbf{b}$. For a_2 and g_2, the XZ WO is translated by $-2\mathbf{b}$, and for a_2' and g_2', by $2\mathbf{b}$. For the Greek-lettered hopping integrals, the two orbitals are on the *same* sublattice. Specifically, the integrals for hopping from xy at the origin to xz at $\pm\mathbf{b}$ are $\alpha_1 \pm \gamma_1$, to xz at $\pm\mathbf{c}$ are $\alpha_2 \pm \gamma_2$, to xz at $\pm(\mathbf{c}+\mathbf{b})$ are $\alpha_3 \pm \gamma_3$, and to xz at $\pm(\mathbf{c}-\mathbf{b})$ are $\alpha_3' \pm \gamma_3'$. Calling γ an electronic dimerization is really a misnomer, because the reason for its existence is simply the difference of relative orientation of the two orbitals. Finally, α_0 is the xy-xz on-site (crystal-field) term.

The parameters dominating the behavior of the $\alpha + a$ Bloch sum are the integral for hopping between the xy and XZ nearest-neighbor WOs, $a_1 = -49$ meV, and the crystal-field term, $\alpha_0 = 31$ meV. Had the former been the only nonvanishing parameter in the $\alpha + a$ Bloch sum, the corresponding term, $2a_1 \cos\pi(k_c - k_b)$, would have killed the peak from the valence-band resonance at $|k_c - k_b|{=}1/2$. So, clearly, this peak—convincingly observed with ARPES—is sensitive to the value of the crystal-field term caused by the ribbon-inversion (see Sec. IIIA in Paper I) and to the details of the xy-XZ and xy-xz hoppings. Note that none of these parameter values were adjusted to fit the ARPES.

7. Synthesis

From the bottom three lines in Fig. 2 we have seen that the k_c-dependencies of the A, G, $\alpha + a$, and $\gamma + g$ Bloch sums of the xz-xz and xy-xz hopping integrals change relatively little for k_b in the $\pm 10\%$ range around $k_F = 1/4$.

By far the strongest k_b-variation of the black $\widetilde{xy}$ bands displayed on the top two lines is the one coming from the denominators of the 3rd resonance terms via $E \approx \tau(k_b)$, to be seen on the 3rd line to the left, in combination with the very different shapes of the V- and C-band residues seen on the 4th line to respectively the left and the right.

What makes the blue resonance peak caused by the edge of the xz V band—seen on the 2nd line to the left near $k_c = 0.75$—differ in shape from the (unhybridized) blue canine-tooth resonance near $k_c = -0.25$ caused by the edge of the xz C band, is the zero of the purple $\alpha + a$ near $k_c = 0.5$ seen on the bottom line. This zero is a bit inside the frame of the dark blue f_V window $(-0.25|0.75)$ and therefore "cuts a hole" in Γ_V on the low-k_c side of the resonance, which is thereby sharpened up. Nothing like this happens for Γ_C near $k_c = -0.25$, because the zero of $\alpha + a$ near -0.1 is outside the f_C window $(-1.25| - 0.25)$. Hence, it is the shape of the canine tooth which is the simpler!

On the other hand, as seen for $k_b = 0.275$ on the 1st line to the left, the backside of the tooth at $k_c = -0.25$ reaches across the ZB at -0.5, where it is crossed symmetrically by the backside of the $\widetilde{xy}(\mathbf{k}+\mathbf{c}^*)$-band tooth caused by the resonance with the yz C band at -0.75. To the right and in black, we now see that strong $(\mathbf{k}, \mathbf{k}+\mathbf{c}^*)$-hybridization around -0.5 merges the canine teeth in the lower band at -0.75 and -0.25, thus resulting in a 60-meV splitting of the two $\widetilde{xy}$ bands.

We can go back and compare with what happens for $k_b = 0.225$. Here, we see on the 2nd line to the left that the blue resonance peak at 0.75 is so sharp that it hardly reaches the ZB at 0.5 and therefore hardly overlaps the peak at 0.25 in the $\widetilde{xy}(\mathbf{k}+\mathbf{c}^*)$ band (seen above on the 1st line) from the yz valence band. Moreover, the hybridization at the zone boundary ZB is much weaker than for $k_b = 0.275$ (black curves to the right on the 2nd line) so that it merely leads to the formation of a bulge in the lower band, 35 meV below the minimum in the upper band between its resonance peaks (1st line to the right).

The zero of the purple $\alpha + a$ near $k_c = 0.5$ which sharpens the peaks from the V bands, also makes the V bands (dark blue and dark green on line 3) contribute nothing to the $(\mathbf{k}, \mathbf{k}+\mathbf{c}^*)$ hybridization at the ZB. The hybridization, therefore, comes exclusively from the C bands and from the dimerization u of the direct, perpendicular hops (red curves to the right on the 2nd line). The blue and the green—equally large—contributions each have a residue given by the value at $k_c = 0.5$ of the gray curve to the right on line 4. For k_b increasing from 0.225 to 0.275, this value increases from 2500 to 3500 meV^2 and thereby enhances the dominating effect of the decreasing denominator.

Finally, we explain why, around $k_c = 0$, the *lower* band is so flat, more than the upper band, and why with increasing k_b this flatness increases and its range decreases.

But first, we explain why the repulsion of the *upper* $\widetilde{xy}$ band by the C band increases far less with k_b than expected from the decrease of the denominators (3rd line, left). The reason is found on lines 4 and 5: For the upper band near $k_c = 0$—which is the $\widetilde{xy}(\mathbf{k}+\mathbf{c}^*)$ band and, hence, the $\widetilde{xy}(\mathbf{k})$ band near ± 1—the light-blue C-band residue $\Gamma_C(k_b, k_c \sim$

± 1) decreases by nearly a factor four for k_b increasing from 0.225 to 0.275, mainly because $\alpha + a$ decreases by almost a factor two. This trend is furthermore enhanced by a nonvanishing repulsion from the V band whose dark-blue residue near $k_c = \pm 1$ hardly changes with k_b and thus becomes more important when $\Gamma_C(k_b, \pm 1)$ is small.

The reason why around $k_c = 0$ the black lower $\widetilde{xy}$ band runs parallel to the red xy band is (see line 2 to the left) that the repulsions from the blue xz and the green yz V bands disperse in opposite directions away from $k_c = 0$, whereby their effects on the dispersion cancel. The reason why the distance of the black band above the red band as well as the k_c extent of its flat part decreases with increasing k_b, is the same as the reason why the blue resonance peak near $k_c = -0.25$ is much smaller than the one near 0.75, namely: that for the dark-blue V-band residues on the 4th line $\Gamma_V(k_b, -0.25)$ is much less than $\Gamma_V(k_b, 0.75)$, and this—in itself—is because the zero of $\alpha + a$ at $k_c = -0.1$ is closer to -0.25 than the zero at 0.5 is to 0.75 (purple curves on line 5). As we now—with k_b increasing—move up in the metallic bands, the V-band perturbation decreases due to the increasing energy denominator and—as the C band is approached—canine teeth growing near $k_c = -0.25$ and 0.25 limit the region over which the lower band is flat.

We conclude that the remarkable asymmetry between the contributions from the V&C bands to the k_c dispersion and splitting of the $\widetilde{xy}$ bands in the gap is mainly due to the difference between the positions of the V&C bands with respect to the structure in the **k**-conserving $\alpha + a$ Bloch sum of the xy-xz hopping integrals. Specifically, the zero of $\alpha + a$ near $k_c = 0.5$ is inside the region where the V band is formed by the $xz(\mathbf{k})$ band—and the C band by the $xz(\mathbf{k} + \mathbf{c}^*)$ band (see dark- and light-blue curves in the figures to the right on line 3)—and not the other way around.

C. Constant-energy contours

On the left-hand side of Fig. 3, we show the upper [Fig. 3(a)], the lower [Fig. 3(b)], and both [Fig. 3(c)] metallic $\widetilde{xy}$ bands in the gap, which extends from -218 meV to $+218$ meV, as functions of (k_b, k_c) in the stripe $0.225 \leqslant k_b \leqslant 0.275$ and $0 \leqslant k_c \leqslant 1$. From the description at the beginning of Sec. II B, we recognize the development of the bands—for k_b increasing—from having strong, upward-pointing resonance peaks near $k_c = 0.75$ and 0.25 in the upper band [Fig. 3(a)], plus a small downward bulge around $k_c = 0.5$ in the lower band [Fig. 3(b)], over having reduced peaks plus a wider and deeper bulge—and minimal width—near midgap, to having strong, downward-pointing resonance peaks (canine teeth) connected by a large bulge in the lower band, plus reminiscences of the upward-pointing resonance peaks in the upper band. The splitting between the two bands [Fig. 3(c)] is smallest at $k_c =$ integer where the $|\mathbf{k}\rangle$ and $|\mathbf{k} + \mathbf{c}^*\rangle$ characters cannot mix and where the direct and indirect hoppings work in opposite directions.

In Fig. 3(d), we show the constant energy contours (CECs) for k_b positive and energies ranging from 100 meV below to 100 meV above the Fermi level which is, itself, 75 meV above the center of the gap. For $E - E_F = -100$ meV, we recognize from the LDA-TB part of Fig. II 10, two notches pointing toward Z in the inner sheet and, in the outer sheet, a bulge centered at the ZB, $k_c = 0.5$. As the energy increases, so does the distance between the bulge and the inner sheet, the notches shrink, and new notches develop in the outer sheet, on either side of the bulge, and pointing toward Y and Y′. It is obviously the resonance peaks pointing upward (downward) in the upper (lower) band which give rise to the notches pointing toward Z (Y and Y′) in the inner (outer) sheets. Along ΓY ($k_c =$ integer), the two sheets are in near contact.

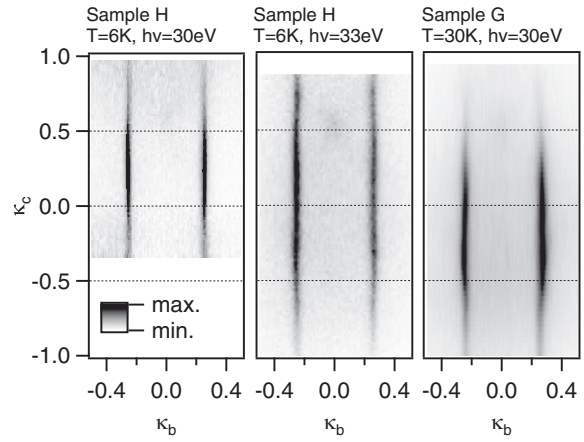

FIG. 4. Three Fermi surfaces out of the data which we use in the following analysis. The two first (similar to Fig. II 9) are from a sample H at $T = 6$ K measured at two photon energies, $h\nu = 30$ eV and 33 eV, corresponding to $\kappa_a = 6.3$ and 6.6, respectively. The last is from a sample G with $h\nu = 30$ eV, $\kappa_a = 6.3$. The figures have been *stretched* along κ_c by a factor 1.7; compare with Figs. II 1 and II 10(b), which are to scale.

Since the quasi-1D bands disperse far more along k_b than along k_c, the shape of two CECs in [Fig. 3(d)] resembles that of the two energy bands in Fig. 1 or in Fig. 2 on the 1st line, to the right. The $E \leftrightarrow k_b$ scaling is approximately: $dE = -\tau'(k_b)dk_b$, with $\tau'(k_b)$ being the dominating part of the Fermi velocity [I (48)]. This resemblance is less good close to the edge of the C or V band where the hybridization with the edge makes the two bands and the two CECs behave differently: Whereas one band remains undistorted, the other gets repelled and, eventually, fuses with the CECs of the edge (see Fig. II 10).

If we interpret a CEC as a doped FS, an energy increase of 50 meV corresponds to a 4% increase of the electron doping, and the undoped FS is the CEC whose k_b averaged over k_c equals 1/4.

We now analyze the ARPES data for energies closer to the Fermi level than the 0.15 eV studied in paper II [2] and identify further features of the theory discussed above.

III. EXPERIMENTAL FERMI SURFACE AND VELOCITIES AND COMPARISON WITH THEORY

In this section we describe our analysis of the ARPES data taken from the intensity cube $I(E, \kappa_b, \kappa_c)$. Figure 4 shows the FS obtained from sample H at $T = 6$ K measured at the two photon energies $h\nu = 30$ eV and 33 eV, which correspond to $\kappa_a = 6.3$ and 6.6, respectively, and from sample G with $h\nu =$

30 eV, $\kappa_a = 6.3$. We know from theory that the FS consists of the four values (left and right, inner and outer sheets) of the Fermi-momentum κ_{Fb} as a function of κ_c when the dispersion with κ_a is neglected.

At first glance the experimental FS does not appear to have inner and outer sheets. However, one can clearly see by eye in Fig. 4 that the black vertical lines (representing the FS) are not exactly straight, but are slightly "breathing" inward and outward in a regular pattern. In the following, we examine this breathing more meticulously. We find that it is the result of our selection rule causing the observed FS to switch from one sheet to the other. Furthermore, the shape of each sheet is found to be consistent with our theory. Nonetheless, as we have shown in past work [8–10] and as discussed further below, we emphasize that the FS is defined by dispersing lineshapes with non-Fermi-liquid features that are generic to the Tomonaga–Luttinger (TL) model. The selection rule explains a puzzle from this past work, that we were able to analyze the lineshapes with a one-band TL spectral theory, even though there are actually two bands. We now understand that for most of k space, ARPES sees only one band at a time. Before presenting and discussing the data in relation to our theory, we discuss the challenges and issues we are facing and explain the method we are using. This method also enables the κ_b-projected Fermi velocity to be extracted as a function of κ_c.

A. Challenges, issues, and methods used for the Fermi-surface determination

1. LiPB-specific issues

As explained in detail in paper II Sec. II [2], the ARPES intensities from the six $t_{2g}(m = yz, xz, xy)$ bands in lithium purple bronze (LiPB) display fine- and coarse-grained variations.

While the two subbands of a given m are periodic in the single zone, the fine-grained intensity modulation considered in paper II Sec. II B1 follows the $|\mathbf{k}\rangle$ character, apart from the nearly canceling phase shifts from the inversion and displacement dimerizations. It is therefore almost periodic in the double zone (Figs. II 1, II 2, and II 3), as if the ribbons had been translationally equivalent (paper I [1], Sec. III A) with the intensity from the lower m band in the first zone and the intensity from the upper m band in the second zone. Due to the dimerization of the ribbons, the m-band is gapped at the physical zone boundary and the shift from one subband to the other of the dominating $|\mathbf{k}\rangle$ character takes place over *a region around* this boundary. This was illustrated in the bottom part of Fig. II 4 for $k_b = 0.225$ and we now repeat this in Fig. 5, but only for $k_b = 0.245$ and the two $\widetilde{xy}$ bands, i.e., those with energies less than ≈100 meV below E_F. The tilde and the dark-red color indicate that these xy-like bands are hybridized with the valence (V) and conduction (C) xz and yz bands which give rise to the peak-, bulge-, and near-contact features first mentioned in Sec. II B 1. The second zone extends from $k_c = -1$ to -0.5 and from 0.5 to 1, with the first zone inserted between them from -0.5 to 0.5. Only near the zone boundaries $k_c = \pm 0.5$ does ARPES see both bands of which the lower has a large bulge whose minimum is split from the upper minimum by as much as 50 meV. The near contact between the two bands [sheets in Fig. 3(d)] at k_c integer is not directly seen in ARPES, because here, one of the bands (sheets) is extinguished, the upper band (inner sheet) at even k_c and the lower band (outer sheet) at odd k_c. The resonance peaks in the upper band are clearly seen at $|k_c| = 0.76$.

Since without the fine-grained ARPES intensity modulation, each band is periodic in the single zone (see Figs. 1 and 2 top line to the right), symmetrization of the ARPES bands around the zone boundaries enabled us in paper II [2] to reconstruct the dispersions continuously (Figs. II 10 and II 11). However, with $h\nu = 30$ eV, the coarse-grained intensity of the $\widetilde{xy}$ bands falls off rapidly for $\kappa_c > 0.5$, and this made it difficult, but—thanks to the fine-grained modulations—not impossible to detect the resonance peaks in the upper band [see Fig. II 14(c2)]. Later, we realized that the spread of the Wannier orbital onto several molybdenums makes the coarse-grained intensity sensitive to the photon energy, which can therefore be chosen to yield good visibility over a sufficiently wide range of κ_c and to produce cancellation between the inversion and displacement phase shifts.

The ARPES intensity from the inner and outer sheets of the FS behaves like the intensity for respectively the upper and lower $\widetilde{xy}$ bands, as we shall see in Fig. 8. For extracting the FS, our present method to be described below, however fails near the zone boundaries because we have no good symmetrization scheme unlike for the bands. We can merely *estimate* the splitting *at* the boundary from the so-called Sparrow criterion used in astronomy [11].

To set the scale, we first recall from the theoretical FS in Fig. 3(d) that even at $k_c = 0.5$, the k_b splitting between the inner and outer sheets amounts to merely $0.01b^*$, i.e., to 2% of the distance between the left- and right-hand FS sheets. The experimental Fig. 4 shows both left- and right-hand sheets and, here, the inner and outer sheets cannot be distinguished because the momentum-distribution widths of the two spectral functions of the bands are larger than their splitting (see paper II, Sec. III B). However, already in the data, we see a slight wrinkle around $\kappa_c = \pm 0.5$ caused by the shift of intensity from one band to the other.

There is a second issue specific to LiPB; it is a quasi-1D material and, at high enough temperatures, manifests a TL-like spectral function with a broad spinon edge feature and a somewhat sharper holon peak feature [9,10,12]. For the data here, the momentum integrated energy distribution curves (EDCs) around k_{Fb} gave a power-law like lineshape (see Fig. 9). Although the LiPB ARPES lineshape is well described by the TL spectral function at high temperature, the spectra do not sharpen as much as expected in the theory [12] at low temperature.[4] Although a phenomenological description [12] of this low-T deviation can be made,[5] we deemed that this description offers no special benefit for the data analysis at hand. Therefore our specific procedure, described below, follows a route in which no theoretical spectral function is forced onto the experimental data.

[4]It might be important here to remind again that, in the TL model, the Fermi momentum k_F remains well defined.

[5]Reference [7] presents a novel and creative microscopic derivation of the phenomenology.

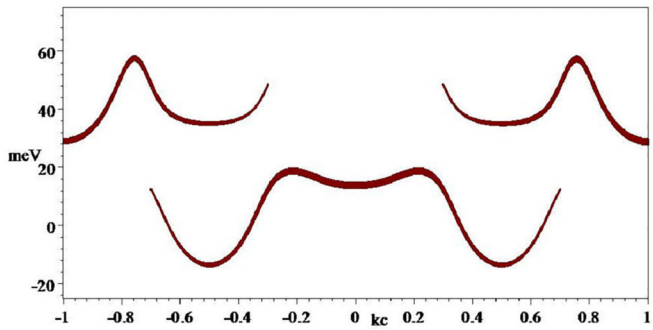

FIG. 5. The $\widetilde{xy}$ bands in the double zone for the two-band Hamiltonian (4) with ARPES-refined TB parameters, like in the bottom panel of Fig. II 4, but only for the dark-red $\widetilde{xy}$ bands, for $k_b = 0.245$, and on an extended energy scale with the upper frame at the Fermi level (75 meV). The fatness is proportional to the fine-grained band-factor ARPES intensity because, for our particular case of $\kappa_a = 6.6$, the dimerization phase shift η [II (9)] is negligible in the k_c region of interest (see Fig. II 2).

2. General issues

Note that the change of momentum in κ_b, visible in Fig. 4, is small—we see that it is in the range of 0.01, which translates to the experimentally very demanding range of 0.012 Å^{-1} using the solid-state definition (ssd) of reciprocal space [see Sec. I (III)]. For our measurements, that is about the size of two detector pixels. We see that it is very possible to extract such a *relative* change from the ARPES data by our method. The determination of the absolute value of the Fermi-momentum and the filling is limited to a systematic error of about 1%.

To obtain the value of the Fermi momentum, one may think that it suffices to determine the peak maximum of the momentum distribution curve (MDC) at E_F. In reality, the *exact* determination of the Fermi momentum is an important issue warranting discussions to be found in, e.g., Refs. [13–17]. There are many intrinsic and extrinsic reasons not to determine the correct k_{Fb}. Particularly important for us is a masking effect in extracting the Fermi momentum, which occurs rather generally and does not depend much on whether the sample is a Fermi liquid, marginal Fermi liquid, or a TL liquid. This effect is sketched in Fig. 6: Even if the ARPES

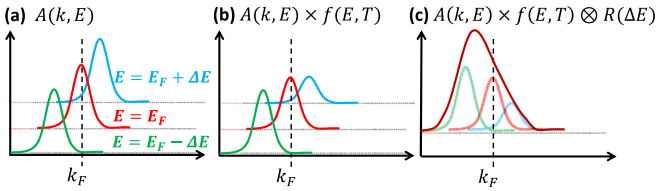

FIG. 6. Sketch to explain a masking effect hindering the Fermi-momentum determination when only considering the maximum of the MDC at E_F. (a) Shown are three MDCs for different energies as indicated around E_F. In panel (a), the spectral function give perfectly symmetric and Lorentzian-like MDCs. The combined effect of (b) the distribution function $f(E)$ and (c) convolution with the energy resolution $R(\Delta E)$ results in an asymmetric lineshape for the MDC at E_F [dark red in panel (c)].

spectral function is perfectly symmetric and Lorentzian-like in the momentum direction [Fig. 6(a)], the combined effects of the distribution function (e.g., the Fermi function) [Fig. 6(b)] and the convolution with the experimental energy resolution [Fig. 6(c)], results in an asymmetric lineshape for MDCs for energies near $E_F \pm \Delta E$. Here, ΔE represents the experimental energy resolution, which for $h\nu = 30$ eV is 16 meV (Sec. III B). Hence, the asymmetry causes the peak momentum to be *inside* the FS.

3. Method

With these considerations in mind, we now explain our methods. It is important to mention again that theory dictates that we cannot distinguish the two bands but obtain an average dispersion weighted by the ARPES band-factor intensity, the $|\mathbf{k}\rangle$ character shown in Fig. 5. This means that, for $|\kappa_c| < 0.35$, we are mainly extracting the outer FS sheet (lower band), while for $0.65 < |\kappa_c|$, we mainly extract the inner sheet (upper band). Thus, like for the bands, the selection rule allows us to distinguish the two FS sheets, except near the zone boundary, $|\kappa_c| = 0.5$, where the intensity shifts from one band to the other. We first discuss, in Sec. III A 3 a, what can be deduced for the zone-boundary situation, using the Sparrow criterion [11] to analyze the MDC widths. This exercise will bring out the fact that the experimental MDC widths greatly exceed the splitting that we wish to determine and thereby make clear the crucial role of the selection rule, which we exploit in Sec. III A 3 b using a so-called dispersion analysis to determine the Fermi momentum as well as the Fermi velocity of separate branches.

Sparrow MDC peak-width analysis. At the zone boundaries, $|\kappa_c| = 0.5$, although we have no way to separate the inner and outer FS sheets, we can nonetheless estimate their possible splitting, as we now describe. As follows from the fine-grained intensity modulation of the two $\widetilde{xy}$ bands discussed in Sec. II (II B 1) and displayed in Fig. 5, the MDC at E_F for $\kappa_c = 0.5$ (or -0.5) is an equally weighted combination of the Lorentzian-like[6] MDCs of both sheets and, as the combination, has the measured total width $\Gamma_{\rm MDC}^{\kappa_c=0.5}$. With this, we can use the so-called Sparrow criterion [11], which states that two identical, separated Lorentzians of the same width $\Gamma_{\rm MDC}^{j=1} = \Gamma_{\rm MDC}^{j=2}$ are indistinguishable if they add up to give a flat top with zero slope and curvature at their center of mass. These conditions allow computing a splitting ($\Delta\kappa_b$) as well as the width of the two Lorentzians ($\Gamma_{\rm MDC}^{1/2}$) from the measured total width ($\Gamma_{\rm MDC}^{\kappa_c=0.5}$). In fact, it will be an upper limit for the splitting and reads $\Delta\kappa_b^{\kappa_c=0.5} = \Gamma_{\rm MDC}^{\kappa_c=0.5}/\sqrt{3}$. The two Lorentzians have a width of $\Gamma_{\rm MDC}^{j} = \Gamma_{\rm MDC}^{\kappa_c=0.5}\sqrt{3}/(1+\sqrt{3})$. The results of this Sparrow analysis are given in Table I and also indicated by the diamonds in Fig. 8. From the table, by seeing that the measured MDC-widths at the zone boundary ($\Gamma_{\rm MDC}^{\kappa_c=\pm0.5}$) and zone center ($\Gamma_{\rm MDC}^{\kappa_c=0}$) are almost the same, we can already see that there is a limit to the determination of the splitting. The MDCs are obviously broad. This broadening is much more than the momentum resolution of the

[6]Here, we use the standard definition of the Lorentzian with $I = \frac{A}{\pi}\frac{\Gamma/2}{(\kappa-\kappa_F)^2+(\Gamma/2)^2}$.

TABLE I. Result of the MDC peak-width analysis (compare also with Fig. 4). The first column gives the individual dataset, the second indicates whether $\kappa_c = +0.5$ or $\kappa_c = -0.5$ was measured. Column 3 gives the Lorentzian width Γ obtained by a line fit and is averaged over both branches, at positive and negative κ_b. Column 4 gives the width of the two Lorentzians (Γ^j_{MDC}) at $\kappa_c = \pm 0.5$ according to the Sparrow criterion. The fifth is the Lorentzian width at $\kappa_c = 0$. The last column, finally, shows the upper limit for the separation in κ_b momentum ($\Delta\kappa_b^{\kappa_c=0.5}$) according to the Sparrow criterion.

Sample		$\Gamma^{\lvert\kappa_c\rvert=0.5}_{\mathrm{MDC}}$	$\Gamma^{j}_{\mathrm{MDC}}$	$\Gamma^{\kappa_c=0}_{\mathrm{MDC}}$	$\Delta\kappa_b^{\lvert\kappa_c\rvert=0.5}$
H 6 K, 30 eV	+	0.030	0.0191	0.031	0.017
H 6 K, 33 eV	+	0.047	0.030	0.051	0.028
	−	0.044	0.028	0.051	0.025
G 30 K, 30 eV	+	0.060	0.038	0.052	0.035
	−	0.051	0.033	0.052	0.030

apparatus [$\Delta\kappa_b \approx 0.005$, see Sec. II (III A)]. The broadening can be for different reasons. There is an *intrinsic* component by the spectral function of the corresponding electron liquid. In the case of a Luttinger-liquid, it is well known (see, e.g., Ref. [18]) that the MDCs are typically sharper, and the EDCs are broader (when compared with a Fermi-liquid). However, there can also be an *extrinsic* component—by an experimental momentum resolution which is not produced by the apparatus alone but, for example, can be caused by the quality of the sample surfaces and the so-called k_z broadening [19,20] that arises from the limited probing depth of the photoelectron. In general, it is hard and requires multiple experiments to distinguish the intrinsic and extrinsic components with full certainty. Looking at the widths for different samples, displayed in Table I, we can believe that there is a larger intrinsic component but also some extrinsic component.

We reiterate that the resulting separation estimate by the Sparrow criterion is an upper limit and the actual splitting has to be below the smallest splitting listed in Table I, resulting in $\Delta\kappa_b^{\kappa_c=0.5} < 0.017$. By taking advantage of the selection rule, we see that this is indeed the case, and we note now that even this upper limit is considerably less than the magnitude of the experimental MDC width at $\kappa_c = 0$, where the selection rule applies and only one branch contributes.

Dispersion analysis. The method used to extract the Fermi momentum κ_{Fb} as a function of κ_c is basically to extrapolate the metallic ARPES band along κ_b for fixed κ_c to the Fermi level (Fig. II 11). The details are sketched in Fig. 7. The experimental dataset is sliced along the κ_c direction; see the slices on the lower part of the figure. Each slice can be seen as a set of so-called momentum distribution curves (MDCs). An MDC [see also Sec. II (IV)] is the photoelectron-intensity at fixed energy, here only dependent on κ_b (see the magenta curves in the upper right of Fig. 7 as examples for MDCs). For the analysis, we choose now to use all MDCs with energies between $E_F - 50$ meV and E_F (the separation ΔE was typically 5 meV). We then fit each MDC (on each dispersion branch) with a Lorentzian. The maximum position of the Lorentzians defines the dispersion (indicated by the purple lines in the upper left of Fig. 7). We interpolated the Fermi-momentum κ_{Fb} by a line fit with the linear function $\kappa_b = (E - E_F)/v_F + \kappa_{Fb}$ (see red line in upper left of Fig. 7). By this line fit we remove the error arising from the masking effect discussed above (see Fig. 6), which appears as a "kink" near the value of the energy resolution.[7] In accordance with the energy resolution of about 16 meV, the kink sets in at (see blue arrow) $E - E_F \approx 13$ meV in Fig. 7.

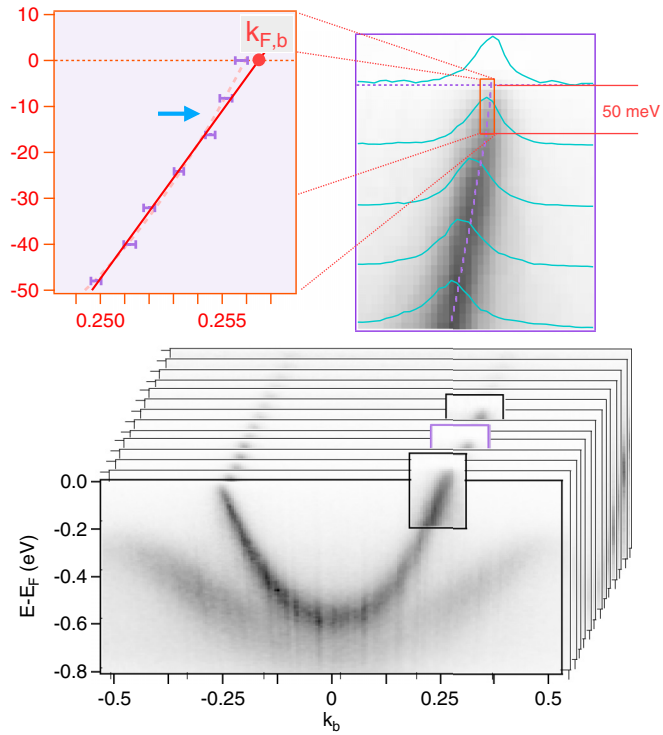

FIG. 7. Method used for the extraction of the Fermi momentum. The experimental dataset is sliced along the κ_c direction (bottom). Each κ_c slice can then be viewed as containing multiple so-called MDCs. The MDCs are intensity curves at fixed energy, dependent only on κ_b (see the magenta curves in the upper right as examples). Then, a line fit with a Lorentzian for all the MDCs between $E_F - 50$ meV and E_F was performed. The maximum of the Lorentzian defines the dispersion $E(\kappa_b, \kappa_c = \mathrm{const})$ (upper left). The Fermi momentum κ_{Fb} is found by linear extrapolation in this interval between $E_F - 50$ meV and E_F (see red extrapolation line and red circle at k_{Fb} in upper left).

The dispersion analysis offers a notable advantage in terms of statistical certainty, primarily due to the utilization of a broader data range spanning 50 meV. For the analysis of TL-liquid performed here, this holds particular significance because the density of states exhibits a power-law decay as it approaches E_F. Furthermore, the dispersion analysis also gives naturally an estimate of the κ_c dependence of the Fermi velocities projected onto the κ_b direction,

$$\mathbf{v}_{F\,j}(k_c) \cdot \mathbf{b}^*/b^* \equiv \partial E_j(k_b, k_c) \big/ (\partial k_b b^*)|_{E_F}. \qquad (11)$$

[7]This "kink" should not be confused with the "kink" resulting from an interaction of a bosonic mode (for an example, see Ref. [21]). Such a bosonic kink for energies lower than the energy of the bosonic mode is bending to the momentum on the unoccupied side because the Fermi velocity is renormalized to smaller values.

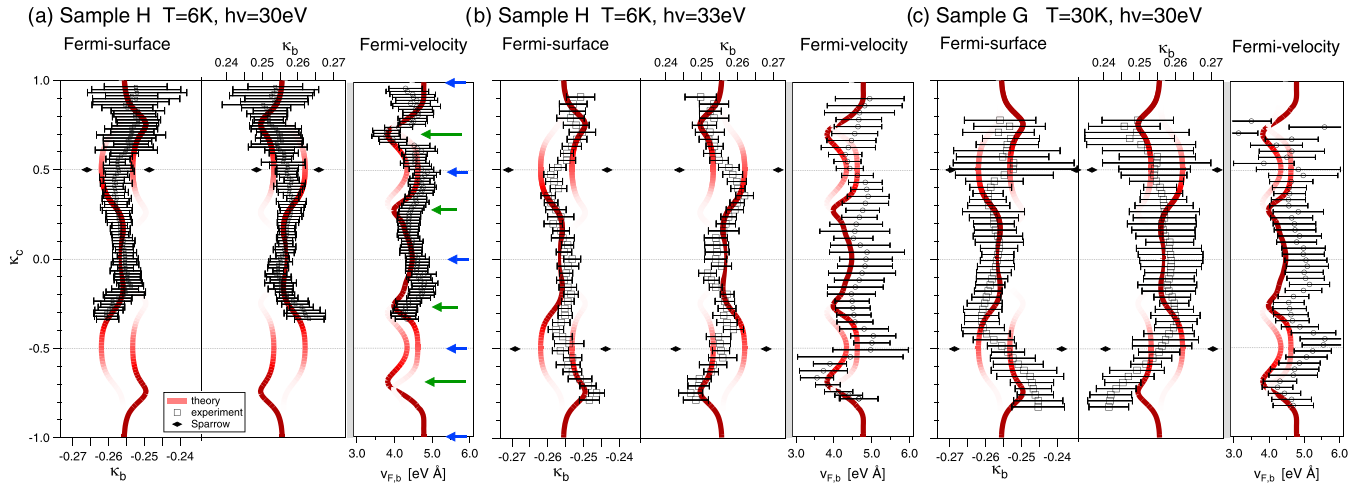

FIG. 8. Results of the Fermi-momentum extraction (black points with error bars, see Sec. III A 3) in the double zone and for each individual dataset, as indicated. For each set, the larger panel shows the four FS sheets (left and right, outer and inner), while the smaller panel shows the k_b-projected velocity (11) averaged using the left and right k_b-projected velocity. Underlayed in dark red with an intensity proportional to the $|\mathbf{k}\rangle$ character [Eq. II (10) with $\eta = 0$, i.e., Eq. I (61)] are the theoretical FS [Fig. 3(d)] and its k_b-projected Fermi velocity. Also included in the graphs for the FS are the results (Table I) of the Sparrow analysis for the maximum splitting at the zone boundary. $\kappa_a = 6.3, 6.6, 6.3$ in respectively panels (a), (b) and (c). Each theoretical and experimental FS has been compressed by a factor 11 along κ_c.

The result of this extraction method is displayed in Fig. 8 and Table II.

B. Results of the Fermi-surface determination and comparison with theory

1. Fermi surface

The result of the Fermi-momentum extraction is displayed in Fig. 8. It compares the experimental FS (black points with error bars) with the theoretical FS (dark-red) calculated using the two-band Hamiltonian (4) with the ARPES-refined parameter values and drawn with the fine-grained intensity proportional to the $|\mathbf{k}\rangle$ character I (60) because, for $\kappa_a = 6.3$ and 6.6, the dimerization phase shift $\eta(\kappa)$ is negligible [see Sec. II (IIB1), Eq. II (10), and Fig. II 2].

We see that the Fermi-momentum extracted from ARPES fits beautifully with the theoretical FS sheet of dominating intensity: In all three measurements, it aligns with the outer sheet for $|\kappa_c| < 0.35$ and with the inner sheet for $|\kappa_c| > 0.65$. Near the zone boundaries, $|\kappa_c| = 0.5$, where the dominating intensity shifts from one sheet to the other, so does the experimentally extracted κ_{Fb}. Also, the general shape of the experimental FS fits nicely with the prediction by theory. This is, on the one hand, not astonishing because we use ARPES-refined parameter values, but on the other hand, the refinement was done for features well away from the Fermi energy, and yet, all details of the theoretical FS [seen in Fig. 3(d) and described in Sec. II C] are seen in the experiment, with the exception of the near contact between the inner and outer sheets, which does require interpolation of the former to $k_c = 0$ or extrapolation of the latter to $k_c = 1$. Later on, we discuss this also for the Fermi velocities.

The experimental upper bound given by the Sparrow criterion on the splitting between the inner and outer sheets at the ZB, $|\kappa_c| = 0.5$, is indicated by the black diamonds. It is consistent with, but considerably larger than, the theoretical splitting.

As can be seen from Table II, for all three samples, k_{Fb} averaged over k_c gives a Luttinger volume which corresponds to an effective $Li_{1.02\pm0.02}$ stoichiometry, i.e., an electron filling of 0.51 ± 0.01. This places the Fermi level 75 meV above the center of the gap in the calculation.

We note that the procedure of refining the values of the TB parameters to fit the ARPES dispersions for energies more than 0.15 eV below E_F in one sample does well in describing the dispersions for energies closer to E_F than 0.15 eV in all three samples. This is a testimonial both to the reproducibility of our findings for samples from different sources and to the essential role that resonant coupling to the higher-energy gapped xz and yz bands plays in determining the dispersion and splitting of the metallic $\widetilde{xy}$ bands.

Finally, we take notice of a very recent publication [22] reporting transport data interpreted as showing a FS reconstruction resulting in a semimetal FS below 100 K. The

TABLE II. Extracted absolute average Fermi momentum k_{Fb}^{avg} (third column) and the Li-stoichiometry from the electron filling (last column). The first column identifies the dataset used, the second column the span of κ_c over which the average was taken (cf. Fig. 8). The error given here is the error of determining the average and does not include the variation of $k_{Fb}(\kappa_c)$ with κ_c. The last column gives the Li stoichiometry from the Luttinger count of the FS, including its error in determination.

Sample	Used κ_c range	k_{Fb}^{avg}	Li stoichiometry
H 6 K, 30 eV	0; 0.995	0.255 ± 0.006	1.02 ± 0.02
H 6 K, 33 eV	−0.785; 0.905	0.254 ± 0.005	1.02 ± 0.02
G 30 K, 30 eV	−0.824; 0.777	0.255 ± 0.008	1.02 ± 0.02
Average		0.255 ± 0.006	1.02 ± 0.02

modeling for this very interesting proposal was based on our analysis, reported in Ref. [23] (Sec. VI E),[8] of possible nesting and gapping of the metallic FS, which, however, concluded that complete spin-density wave gapping requires an effective exchange interaction about three times the value given by the local spin-density approximation (LSDA) and is therefore unlikely.

We point out, as is also acknowledged in Ref. [22], that the 6 K ARPES data reported here and in Ref. [23] do not show any evidence for such a FS reconstruction and that our measured Fermi velocity ($\approx$4.6 eV Å $\approx 7 \times 10^5$ m/s) which was shown as the slope of the unreconstructed, weak bands in Fig. 15 of Ref. [23] and of the dashed bands in Fig. S10(c) of Ref. [22], is several times larger than those ($\approx 2 \times 10^5$ m/s $\approx$ 1.3 eV Å) for the gapped bands at the Fermi level in Figs. 15 and S10(c).

2. *Fermi velocity*

To the right of each FS in Fig. 8, we show the k_c dependence of the k_b-projected Fermi velocity, defined by Eq. (11): in black, as extracted from ARPES, and in red, as calculated with the two-band Hamiltonian.[9]

Overall, we see a good qualitative correspondence between the theoretical and the experimentally extracted values. For those k_c values where the k_b direction is normal to the FS, the velocity projection (11) has extrema. At the zone centers (k_c = integer) and zone boundaries ($|k_c| = 0.5$) – indicated by blue arrows in Fig. 8 – these extrema are flat maxima. For the inner-sheet (upper-band) notches (long green arrows at $|k_c| \approx 0.75$), the extrema are deep *minima*. Also the outer sheet (lower band) has velocity minima (short green arrows at $|k_c| \approx 0.30$). Their origins are the weak resonance peaks at $|k_c| \approx 0.25$ [see Fig. 5 and Eq. (10)], combined with the increase of $|\mathbf{k}\rangle$-$|\mathbf{k} + \mathbf{c}^*\rangle$ hybridization and the concomitant formation of bulges as the zone boundaries at $|k_c| = 0.5$ are approached.

The velocity of the outer sheet (lower band) decreases from 4.5 eV Å at the zone center ($k_c = 0$) to the 4.0 eV Å deep minima near $|k_c| = 0.30$ and rises again to the 4.6 eV Å maxima at the centers of the bulges, $|k_c| = 0.5$. For the inner sheet (outer band), the velocity decreases from 4.7 eV Å at the zone centers ($|k_c| = 1$), to 3.9 eV Å deep minima near the notches and rises again to 4.3 eV Å maxima at the zone boundaries. These sheet- and k_c-dependent values may be compared with the dominating value 4.6 eV Å of $b\tau'(k_b)$ in Eqs. I (50) and I (48) from the direct hopping along the ribbon. Due to the indirect hops via the valence and conduction bands giving rise to the resonance terms in Eq. (4), the band and k_c average of the velocity projections is smaller than $b\tau'(k_b)$. The velocities extracted from the ARPES data (black) clearly show both the qualitative behavior and the general magnitude implied by the theory (dark red). To a small extent, this is expected since, as explained in Sec. I (IV) and specified in Eqs. I (43) and I (45), a few of the many LDA TB parameters were refined to make the bands agree with the large- but not the small-energy features of the ARPES bands.

It is also interesting for the many-body physics of LiPB to compare the experimental velocities to those for the TB bands based on the LDA parameters. The LDA dominant velocity value is[10] 4.0 eV Å. The experimental velocities (and those for the ARPES-refined TB) are generally greater than those for the LDA[11] by about 15%.

There are two points to be made. First, for a three-dimensional (3D) quasiparticle material the increase of the experimental velocity relative to the LDA value would seem surprising since the usual effect [24], arising from an energy-dependent single-particle self-energy, e.g., caused by *e*-*e* or *e*-phonon interactions, is an *in*crease of the Fermi *mass*, i.e., a decrease of the Fermi velocity.[12] Indeed, such was found in the single-site dynamical mean-field theory (DMFT) quasiparticle treatment of LiPB [27]. However, LiPB is a quasi-1D material whose ARPES k-averaged lineshapes show TL-model properties, i.e., quasiparticle suppression and spin-charge separation. Specifically, the holon-peak and spinon-edge features disperse with different velocities, v_ρ and v_σ, respectively [18,28,29]. Our model-independent ARPES analysis procedure, if performed on a TL-lineshape, would yield a dispersion intermediate between v_ρ and v_σ, but tending mostly to that of the holon peak. Within one-dimensional (1D) theory, v_ρ and v_σ can just as well be either larger or smaller than the underlying v_F of a noninteracting system, as can be seen, for example from formulas within the framework of the "g-ology" formulation [18,30]. So if we identify the LDA value of $v_F = 4.0$ eV Å as "noninteracting," which ignores the difficulty of disentangling any many-body contribution already present in LDA, and think of our ARPES lineshape in a TL context, it is well within general theoretical expectations that our experimental velocity is larger than the LDA value. In this view, it may well be that our ARPES-refined TB description is modifying the entire k_b dispersion somewhat in order to reproduce the experimental low-energy scale velocity near E_F.

Second, combining our results with a previous ARPES lineshape analysis [8], we can be somewhat more precise about the velocity renormalizations for LiPB. At high temperatures, where the LiPB ARPES lineshapes are well described by TL lineshape theory [29] for nonzero T, the best TL

[8]This section was deleted before resubmission to Phys. Rev. B at the insistence of one of two referees.

[9]The velocity projections of Eq. (11) were calculated as differences between the bands for $k_b = 0.2505$ and 0.2495.

[10]Calculated from $b\tau'(k_b)$ and also given in Eq. I (50).

[11]The band- and k_c-resolved velocities which result from using the shifted and the straight LDA parameters (see Fig. 12) have averages more than 15% below that of the experimental velocities in Fig. 8, and they have much larger variations: Near $k_c = 0$ and 0.5 the LDA velocities do lie around the 15% lower LDA value, 4.0 eV Å, but for intermediate values of k_c, they vary much more, reaching minima at 3.4 and 3.0 eV Å for respectively the upper and lower bands (inner and outer sheets) in the shifted LDA and, in the straight LDA, minima at 2.5 eV Å and 3.3 eV Å% with the deeper minimum now for the upper band.

[12]For quasiparticles, one would invoke a very strong k dependence of the self-energy to understand a decrease of the mass, as discussed, e.g., in Refs. [25] and [26].

description [8] for the Γ-Y ($k_c = 0$) ARPES lineshapes was achieved for $v_\rho/v_\sigma = 2$. At that time no definitive LDA value of v_F was available. If we now think of our ARPES velocity as being nearly that of v_ρ and take our LDA velocity as an underlying noninteracting v_F, then—at least for ΓY—we conclude that v_ρ is roughly $1.15v_F$, and that v_σ is roughly $0.6v_F$.[13] A 1D Hubbard-model analysis [5] estimated $v_\sigma/v_F \approx J/2\tau$ with $J \approx 0.2$ eV being an effective superexchange interaction, and $\tau \approx 0.8$ eV being the primary k_b hopping, implying $v_\sigma/v_F \approx 1/8$.

3. Connecting to the Tomonaga-Luttinger critical exponent α

As already stated in the introduction of paper I [1], LiPB displays Luttinger-liquid properties. Most remarkably, although the FS is well defined and could be extracted above, the lineshapes are better described by a TL spectral function. Nevertheless, there are also substantial T-dependent departures from the TL model. The ARPES lineshapes at temperatures 250 to 300 K are well described by the TL spectral function, showing both spinon and holon features (broadened by temperature and experimental resolution). With decreasing T the exponent varies with T, from $\alpha = 0.9$ at 250 K to 0.6 at 50 K, and also, the ARPES lineshape no longer agrees with the TL lineshape, although it does continue to display quantum critical scaling, a characteristic 1D property [9]. The spectra for k integration along the quasi-1D direction, for temperatures $T = 4$ K and 30 K and resolution 5 meV are well described by a power law with $\alpha = 0.7$ [10].

In the following, we repeat the analysis of Ref. [10] with our recent datasets used to determine the FS above. However, in the course of the present study, we found that (i) all previous TB ladder models are very unrealistic, and (ii) the detectable bands of ARPES vary with fine-grained intensity proportional to the $|\mathbf{k}\rangle$ character. In principle, these findings should inform the choice of a particular TL model. For the phenomenological extraction of the α value, however, we still use the same procedure as in Ref. [10] to obtain its value. As before, we use the κ-integrated spectral weight of a one-band, spin-rotational invariant TL model [29] with $v_\rho/v_\sigma = 2$. The theoretical spectrum was broadened by the experimental energy resolution of 16 meV.

The data displayed in Fig. 9 are integrated over κ_b and κ_c (cf. Fig. 4). For the κ_c direction, the data are integrated over two intervals, according to whether the dominant character is $|\mathbf{k}\rangle$ or $|\mathbf{k}+\mathbf{c}^*\rangle$. As visible in Fig. 9, sample G ($T = 30$ K) shows a typical value of $\alpha = 0.70$ for both intervals. The data for sample H ($T = 6$ K) vary a bit more on the two intervals but are still within the error range, yielding on average

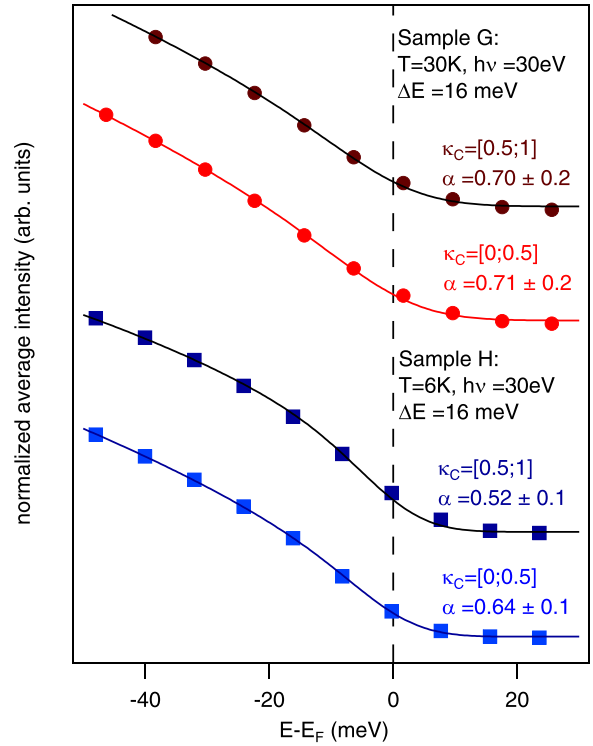

FIG. 9. Analysis of the TL exponent of the data for sample G ($T = 30$ K) and H ($T = 6$ K). The FSs are presented in Fig. 4. Here the data are momentum-integrated over two intervals, where the dominating band character is either $|\mathbf{k}\rangle$ or $|\mathbf{k}+\mathbf{c}\rangle^*$.

$\alpha = 0.58$. Connecting to the study of Ref. [9], despite a considerable difference in the determined α values for samples G and H, these values are within the α ranges of former studies. To shed light on more details, temperature-dependent measurements in the full range of relevant momenta would be required as well as the usage of a more realistic TL model than the one-band, spin-rotational invariant TL model for the line fit.

IV. INTERACTIONS AND CORRELATIONS

As described in the first paragraph of paper I [1], for interacting electrons that can only propagate in one spatial dimension, Landaus Fermi-liquid (FL) theory does not hold [28,31,32]. Instead one finds a correlated Luttinger-liquid (LL) system with a zero density of states at the Fermi energy. Furthermore, the density of states increases at finite energy away from the Fermi energy following a Tomonaga-Luttinger (TL) model lineshape characterized by an anomalous exponent α. As shown in Figs. I 1 and 9, we indeed observe such a lineshape of the density of states below the Fermi energy in $LiMo_6O_{17}$. Although this LL behavior occurs for even an infinitesimally small Coulomb interaction, nonetheless the actual magnitude—and also the range—of the interaction is important because these determine the values of correlation function power laws such as α, as well as other possible properties of the actual interacting state in any particular material. Thus it is generally important to try to make an estimate of the interaction strength and range.

[13] We take cognizance that the previous high-T, Γ-Y, TL lineshape analysis [8] found $v_\rho = 4.0$ eV Å, coincidentally, we think, the same as our LDA value. That our present value of roughly 4.6 eV Å along Γ-Y ($k_c = 0$) is somewhat larger could perhaps be due to the considerable temperature difference (250 K vs 6 K), the considerable difference in the analyzer angle resolutions along k_b (0.016 Å^{-1} in the early work vs 0.006 Å^{-1} in the present work), or perhaps some small sample dependence. In any case the ratio $v_\rho/v_\sigma \approx 2$ is essentially the same for the present lineshapes and the text conclusion that v_ρ is nontrivially larger than v_F is unaltered.

Using constrained density-functional theory (DFT), Popovic and Satpathy [4] showed that the Coulomb interaction U between two electrons in atomic d-like orbitals of Mo in LiPB is $U_{\text{Mo-}d} = 6.4\,\text{eV}$. Constrained RPA calculations for a dense fcc lattice of atomic Mo yield a value of $U_{\text{Mo-}t_{2g}} = 3.7$ eV for the atomic-like t_{2g} orbitals of a single Mo atom [33]. However, it is important to realize that the Wannier orbitals that build the one-dimensional bands are far from being atomic and localized on a single Mo atom. As we showed, the smallest tight-binding model one can make for $LiMo_6O_{17}$ considers six bands per unit cell, and the resulting Wannier orbitals spread over several unit cells (see Figs. I 5 and I 9). Thus, the parameter determining the Coulomb interaction strength for the Wannier orbitals will be smaller than the Coulomb parameter for a single atomic Mo orbital, due both to the dilution of the charge density to several Mo atoms and to screening. Calculating the screened Coulomb interaction between such large Wannier orbitals for a material with many atoms per unit cell is a daunting task. Neither accurate constrained random-phase approximation nor constrained density-functional theory calculations seem feasible with the currently available codes.

While it is computationally difficult to reliably calculate the screened Coulomb interaction of such large Wannier orbitals, one can very well calculate the bare Coulomb interaction. We have made this calculation and the result is $U^{\text{Bare}}_{\text{Mo-}W_{xy}} = 2$ eV. We can easily rationalize this result by noting that the bare Coulomb interaction (F0) for the atomic $4d$ orbitals in Mo is $U^{\text{Bare}}_{\text{Mo-}d} = 12.5$ eV and that the Wannier orbitals in LiPB are spread over several (5+) Mo atoms. Due to the large spread of the Wannier function, the bare value of the nearest-neighbor Coulomb interaction V (and also those for even further distant neighbors) will be smaller but still sizable compared with U. Noting that the bare value of $U^{\text{Bare}}_{\text{Cu-}d} = 25$ eV for strongly correlated cuprates and is $U^{\text{Bare}}_{\text{C-}p} = 14$ eV for graphene gives a useful perspective on the much smaller value of the bare U in LiPB. We should warn the reader here that this value $U^{\text{Bare}}_{\text{Mo-}W_{xy}} = 2$ eV is not the value one should use in a model calculation. The bare interaction sets a clear upper limit but should be greatly reduced in the material due to solid-state screening. As a guide to the possible magnitude of the screening effect, we note again that Popovic and Satpathy calculated a screened value of 6.4 eV for atomic Mo in LiPB, roughly half the bare atomic value $U^{\text{Bare}}_{\text{Mo-}d} = 12.5$ eV. A similar screening reduction down from the bare 2 eV value for our Wannier orbitals is expected.

The small value of the Coulomb interaction between the extended Wannier orbitals also explains why we experimentally find that the xz (yz) and XZ (YZ) bonding orbitals are doubly occupied forming an $S = 0$ state instead of favoring a Hund's rule ground-state triplet state with $S = 1$ where one electron is in the xz (XZ) orbital and one electron in the yz (YZ) orbital with parallel spin. One should not compare the gap $4G_1 \approx 400\,\text{meV}$ [Eqs. I (29), I (35), and I (45)] to the bare atomic interaction strength, but to the greatly reduced interaction strength of the Wannier functions due to the spread of the Wannier function over several Mo atoms within the unit cell.

For LiPB there are a number of previous theoretical studies aimed at understanding its various interesting strongly correlated quasi-1D properties [5–7,34–39]. Some of the various studies take specific values for U- and V-type interactions, for U in a range from the Popovic-Satpathy value of 6.4 eV down to 1 eV, and for V-type interactions in the range 0.5 to 1 eV. It is not our purpose here to give any critique of these various models, which are elegant and creative, but the magnitude of the Coulomb interaction for our Wannier orbitals is supportive of the models which take U at the low end of the range. The experimental $\alpha > 1/2$ can be rationalized with both large and small values of U [6,35], but in so doing, a role for V-type neighbor interactions is essential, because for a simple single-chain Hubbard model the maximum value of $\alpha = 1/8$ is obtained only for infinite U. The V-type values used are all generally consistent with our findings.

We note that Ref. [27], using the variational cluster approximation (VCA) and dynamical mean-field theory (DMFT), found that, for values of U_{Mott} exceeding 0.7 and 2.5 eV, respectively, a Mott-Hubbard gap opens in their LDA bands, glaringly inconsistent with experiment, and therefore giving a clear upper limit. They note that the DMFT (VCA) overestimates (underestimates) U_{Mott}, so the two methods provide a range for an upper limit on U for the four-orbital set of Ref. [27]. Roughly, we expect that a set reduced in size by a factor of n will be n times less localized, with U about n times smaller, implying for our final two-orbital set a general reduction in Coulomb energies by a factor of $2/4 = 1/2$, relative to the four-orbital set of Ref. [27]. Thus our conclusion on the smallness of U is generally consistent with the findings of Ref. [27].

Reference [27] also emphasized that the two metallic bands are half filled. This question is important because most of the theories cited above assume no b dimerization, i.e., assume that Mo(1) and Mo(4) are equivalent, and thereby view the two metallic bands as being quarter-filled. We agree with this emphasis in Ref. [27], in the sense that the dimerization gap is 0.7 eV, nearly 20% of the entire bandwidth [see Sec. I (III B)]. But there is some nuance. The motivation in the theoretical models is to make contact with a property of the quarter-filled Hubbard model, that of so-called $4k_F$ charge fluctuations, or even charge ordering, resulting from the V-type interactions. Dimerization is known to greatly diminish the tendency to such charge fluctuations [40], i.e., the two compete. The fact that the estimated magnitudes of the V-type interactions are in fact comparable to the dimerization gap implies that the relevance of the quarter-filling scenarios is not ruled out, presumably depending on details. So on the theory side, further assessment using more realistic modeling is essential. On the experimental side, Ref. [6] proposes measurements to directly search for the $4k_F$ charge fluctuations.

V. CONCLUSION AND IMPLICATIONS

In conclusion, we have presented in great detail the electronic structure of $LiMo_6O_{17}$ that is experimentally obtainable using ARPES, emphasizing the degree of one-dimensional behavior of the bands in the vicinity of E_F and the excellent overall agreement with the LDA band structure.

With the aim of fully describing and understanding the metallic bands found in the ARPES experiment, especially the details of FS splitting and warping, the LDA electronic structure was downfolded to a tight-binding description with the three Mo1-centered t_{2g} Wannier orbitals (WOs) per formula unit [Sec. I (VI)] using the newly developed full-potential version of the order-N muffin tin orbital method [Sec. I (II)]. This description is based on analyzing the LiPB crystal structure as built from corner-sharing MoO_6 octahedra forming a staircase running along **c** of biribbons extending along **b** [Sec. I (III)].

The six t_{2g} WOs per primitive cell accurately describe not only the four bands seen by ARPES, but all six bands in the 1 eV neighborhood of E_F. This band structure [Sec. I (IV) and Fig. I 4] is basically two-dimensional and formed by the xy, xz, and yz WOs (Fig. I 9) giving rise to three 1D bands running along, respectively, **b**, **c**+**b**, and **c**−**b**, i.e., at a 120° angle to the two other bands (Figs. I 8 and II 10). The dimerization from $c/2$ to c of the ribbons into biribbons gaps the xz and yz bands and leaves the xy band metallic in the gap, but resonantly coupled to its edges and, hence, to the **c**+**b** and **c**−**b** directions. Inclusion of the xz and yz bands are indispensable in describing the strong indirect contributions to the k_c dispersion and splitting of the metallic xy bands. These are most prominent (see Figs. I 8, II 10, and 8) at the crossing of the xy-band CECs running parallel to the $P_1Q_1P_1'$-line ($k_b = 0.225$) in reciprocal space with those of the xz and yz V&C-band edges along, respectively, ZY′ and ZY. All the ARPES-measured dispersions, as well as the FS, indeed confirm the resonant indirect couplings and thus the essential need for the six-band picture. The TB bands are very well described by an analytic 6×6 Hamiltonian I (35) or I (56) with parameters optimized to match the ARPES data for energies more than 0.15 eV below E_F. Finally, the mix of direct and resonant indirect couplings along the **c** direction can be explicitly displayed by further analytical downfolding to the effective 2×2 Hamiltonian (4). This and direct observation by ARPES is compelling evidence for the existence of pronounced resonance structures near E_F in LiPB.

In Sec. IV, we have presented some implications of our results specifically regarding interactions and correlations. In addition, there are four important implications for the general questions posed in the introduction of paper I [1]. These implications follow directly from the central content of the paper, our new knowledge, and understanding of the size of the splitting and perpendicular dispersions of the quasi-1D bands in the gap (Figs. 1 and 2), especially the indirect resonance contributions. They have been stated already in the flow of the presentation, and we merely summarize them here.

First, the reality of the resonance contributions casts serious doubts on theoretical descriptions based on TB bands, which are featureless like the red ones in Figs. 1 and 2, i.e., casts doubt on all previous TB and TL models. Furthermore, in constructing an appropriate many-body Hamiltonian, it should be taken into serious consideration that, with ARPES, we have now been able to follow the resonance peak induced by the valence band to energies nearly 150 meV below the Fermi level (Fig. II 10) and, there, find the peak to have a magnitude of about 50 meV, as predicted by the LDA, cf. Fig. II 14(c2).

Second, the general magnitude of the $t_\perp$ hoppings would suggest that 1D-to-3D crossover should occur for T as high as at least 150 K, unless thwarted by the theoretically expected strong downward low-T renormalization due to LL fluctuations on the chains, as pointed out in the introduction. However, the good agreement between LDA and ARPES data at $T = 6$ K implies that this renormalization does not take place. This circumstance is not only puzzling, given the evidence for LL effects on the chains at high T, but eliminates one very attractive explanation for the exceptional stability of quasi-1D behavior in this material. Our new quantitative knowledge of the $t_\perp$ hoppings further emphasizes this puzzle.

Third, the coupling of the quasi-1D bands to the V&C bands causes the details of the FS splitting and warping (Figs. 3 and 8) to depend strongly on the position of E_F, which in turn depends on the Li concentration. This implies that any property sensitive to the details of the FS will be very sensitive to the stoichiometry. One can then speculate that this FS sensitivity is connected to the sample dependence of the superconductor (SC), especially if the SC is the product of the quasi-1D nature of the FS. We have already noted that the actual position of E_F in LiPB is such as to maximize the quasi-1D nature of the FS. This could be an important addition to the various previous theories of the SC [35–39].

Fourth, the spatial dependence of the $t_\perp$ hoppings argues strongly against coupled ladder models of the chains. At the simplest level, the magnitude of the direct terms for hoppings within and between biribbons [Sec. I (IV)] differ by less than a factor of two, respectively, $t_{\perp,1} \equiv -(t_1 + u_1) = 14$ meV and $t_{\perp,2} \equiv -(t_1 - u_1) = 8$ meV. Just this would leave the ladders not very well defined as separable objects. But, much more importantly, the range of the indirect contributions is at least an *order of magnitude* longer and even depends crucially on the position of the $\widetilde{xy}$ bands in the gap (Sec. II). We conclude that modeling the chains as separable, weakly coupled ladders is very unrealistic.

To conclude, our results offer both a strong motivation and a concrete framework for a serious reappraisal of the extent to which the various past many-body models capture the actual measured one-electron electronic structure of LiPB sufficiently well to be trusted for rationalizing its fascinating quasi-1D, many-body, coupled-chain physics. The efforts to understand the resulting behavior are still ongoing, and we hope that our new knowledge and highly portable description of the one-electron electronic structure will contribute to this effort.

[1] L. Dudy, J. W. Allen, J. D. Denlinger, J. He, M. Greenblatt, M. W. Haverkort, Y. Nohara, and O. K. Andersen, companion paper, Phys. Rev. B **109**, 115143 (2024).

[2] L. Dudy, J. W. Allen, J. D. Denlinger, J. He, M. Greenblatt, M. W. Haverkort, Y. Nohara, and O. K. Andersen, companion paper, Phys. Rev. B **109**, 115144 (2024).

[3] P. Löwdin, J. Chem. Phys. **19**, 1396 (1951).
[4] Z. S. Popovic and S. Satpathy, Phys. Rev. B **74**, 045117 (2006).
[5] P. Chudzinski, T. Jarlborg, and T. Giamarchi, Phys. Rev. B **86**, 075147 (2012).
[6] J. Merino and J. V. Alvarez, Phys. Rev. B **91**, 035135 (2015).
[7] P. Chudziński, Eur. Phys. J. B **90**, 148 (2017).
[8] G.-H. Gweon, J. W. Allen, and J. D. Denlinger, Phys. Rev. B **68**, 195117 (2003).
[9] F. Wang, J. V. Alvarez, S.-K. Mo, J. W. Allen, G.-H. Gweon, J. He, R. Jin, D. Mandrus, and H. Höchst, Phys. Rev. Lett. **96**, 196403 (2006).
[10] L. Dudy, J. D. Denlinger, J. W. Allen, F. Wang, J. He, D. Hitchcock, A. Sekiyama, and S. Suga, J. Phys.: Condens. Matter **25**, 014007 (2013).
[11] A. Jones, J. Bland-Hawthorn, and P. Shopbell, in *Astronomical Data Analysis Software and Systems IV, ASP Conference Series* (1995), Vol. 77, p. 503.
[12] F. Wang, J. V. Alvarez, J. W. Allen, S.-K. Mo, J. He, R. Jin, D. Mandrus, and H. Höchst, Phys. Rev. Lett. **103**, 136401 (2009).
[13] M. Lindroos and A. Bansil, Phys. Rev. Lett. **77**, 2985 (1996).
[14] V. N. Strocov, R. Claessen, G. Nicolay, S. Hüfner, A. Kimura, A. Harasawa, S. Shin, A. Kakizaki, P. O. Nilsson, H. I. Starnberg, and P. Blaha, Phys. Rev. Lett. **81**, 4943 (1998).
[15] L. Kipp, K. Roßnagel, C. Solterbeck, T. Strasser, W. Schattke, and M. Skibowski, Phys. Rev. Lett. **83**, 5551 (1999).
[16] A. Kaminski and H. M. Fretwell, New J. Phys. **7**, 98 (2005).
[17] V. Brouet, A. Nicolaou, M. Zacchigna, A. Taleb-Ibrahimi, P. Le Fèvre, and F. Bertran, J. Electron Spectrosc. Relat. Phenom. **185**, 146 (2012).
[18] J. Voit, J. Phys.: Condens. Matter **5**, 8305 (1993).
[19] T. Grandke, L. Ley, and M. Cardona, Phys. Rev. B **18**, 3847 (1978).
[20] V. Strocov, J. Electron Spectrosc. Relat. Phenom. **130**, 65 (2003).
[21] A. Lanzara, P. V. Bogdanov, X. J. Zhou, S. A. Kellar, D. L. Feng, E. D. Lu, T. Yoshida, H. Eisaki, A. Fujimori, K. Kishio, J.-I. Shimoyama, T. Noda, S. Uchida, Z. Hussain, and Z.-X. Shen, Nature (London) **412**, 510 (2001).
[22] J. L. Cohn, C. A. M. dos Santos, and J. J. Neumeier, Phys. Rev. B **108**, L100512 (2023).
[23] L. Dudy, J. Allen, J. Denlinger, J. He, M. Greenblatt, M. Haverkort, Y. Nohara, and O. K. Andersen, arXiv:1812.03388v1.
[24] A. Mackintosh and O. K. Andersen, *The Electronic Structure of Transition Metals* (Cambridge University Press, Cambridge, 1980), Chap. Electrons at the Fermi surface, pp. 149–224.
[25] T. Miyake, C. Martins, R. Sakuma, and F. Aryasetiawan, Phys. Rev. B **87**, 115110 (2013).
[26] C. H. P. Wen, H. C. Xu, Q. Yao, R. Peng, X. H. Niu, Q. Y. Chen, Z. T. Liu, D. W. Shen, Q. Song, X. Lou, Y. F. Fang, X. S. Liu, Y. H. Song, Y. J. Jiao, T. F. Duan, H. H. Wen, P. Dudin, G. Kotliar, Z. P. Yin, and D. L. Feng, Phys. Rev. Lett. **121**, 117002 (2018).
[27] M. Nuss and M. Aichhorn, Phys. Rev. B **89**, 045125 (2014).
[28] T. Giamarchi, *Quantum Physics in One Dimension* (Oxford University Press, 2004).
[29] D. Orgad, Philos. Mag. B **81**, 377 (2001).
[30] J. Solyom, Adv. Phys. **28**, 201 (1979).
[31] J. M. Luttinger, J. Math. Phys. **4**, 1154 (1963).
[32] S.-i. Tomonaga, Prog. Theor. Phys. **5**, 544 (1950).
[33] E. Şaşıoğlu, C. Friedrich, and S. Blügel, Phys. Rev. B **83**, 121101(R) (2011).
[34] J. Merino and R. H. McKenzie, Phys. Rev. B **85**, 235128 (2012).
[35] W. Cho, C. Platt, R. H. McKenzie, and S. Raghu, Phys. Rev. B **92**, 134514 (2015).
[36] N. Lera and J. V. Alvarez, Phys. Rev. B **92**, 174523 (2015).
[37] C. Platt, W. Cho, R. H. McKenzie, R. Thomale, and S. Raghu, Phys. Rev. B **93**, 214515 (2016).
[38] O. Sepper and A. G. Lebed, Phys. Rev. B **88**, 094520 (2013).
[39] A. G. Lebed and O. Sepper, Phys. Rev. B **87**, 100511(R) (2013).
[40] S. Ejima, F. Gebhard, and S. Nishimoto, Phys. Rev. B **74**, 245110 (2006).